

# NO MORE ACTIVE GALACTIC NUCLEI IN CLUMPY DISKS THAN IN SMOOTH GALAXIES AT $Z \sim 2$ IN CANDELS / 3D-HST\*

JONATHAN R. TRUMP,<sup>1,†</sup> GUILLERMO BARRO,<sup>2</sup> STÉPHANIE JUNEAU,<sup>3</sup> BENJAMIN J. WEINER,<sup>4</sup> BIN LUO,<sup>1</sup> GABRIEL B. BRAMMER,<sup>5</sup> ERIC F. BELL,<sup>6</sup> W. NIEL BRANDT,<sup>1</sup> AVISHAI DEKEL,<sup>7</sup> YICHENG GUO,<sup>2</sup> PHILIP F. HOPKINS,<sup>8</sup> DAVID C. KOO,<sup>2</sup> DALE D. KOCEVSKI,<sup>9</sup> DANIEL H. MCINTOSH,<sup>10</sup> IVELINA MOMCHEVA,<sup>11</sup> S. M. FABER,<sup>2</sup> HENRY C. FERGUSON,<sup>5</sup> NORMAN A. GROGIN,<sup>5</sup> JEYHAN KARTALTEPE,<sup>5</sup> ANTON M. KOEKEMOER,<sup>5</sup> JENNIFER LOTZ,<sup>5</sup> MICHAEL MASEDA,<sup>12</sup> MARK MOZENA,<sup>2</sup> KIRPAL NANDRA,<sup>13</sup> DAVID J. ROSARIO,<sup>13</sup> AND GREGORY R. ZEIMANN<sup>1</sup>

*Draft version June 17, 2021*

## ABSTRACT

We use CANDELS imaging, 3D-HST spectroscopy, and Chandra X-ray data to investigate if active galactic nuclei (AGNs) are preferentially fueled by violent disk instabilities funneling gas into galaxy centers at  $1.3 < z < 2.4$ . We select galaxies undergoing gravitational instabilities using the number of clumps and degree of patchiness as proxies. The CANDELS visual classification system is used to identify 44 clumpy disk galaxies, along with mass-matched comparison samples of smooth and intermediate morphology galaxies. We note that, despite being mass-matched and having similar star formation rates, the smoother galaxies tend to be smaller disks with more prominent bulges compared to the clumpy galaxies. The lack of smooth extended disks is probably a general feature of the  $z \sim 2$  galaxy population, and means we cannot directly compare with the clumpy and smooth extended disks observed at lower redshift. We find that  $z \sim 2$  clumpy galaxies have slightly enhanced AGN fractions selected by integrated line ratios (in the mass-excitation method), but the spatially resolved line ratios indicate this is likely due to extended phenomena rather than nuclear AGNs. Meanwhile the X-ray data show that clumpy, smooth, and intermediate galaxies have nearly indistinguishable AGN fractions derived from both individual detections and stacked non-detections. The data demonstrate that AGN fueling modes at  $z \sim 1.85$  - whether violent disk instabilities or secular processes - are as efficient in smooth galaxies as they are in clumpy galaxies.

*Subject headings:* galaxies: active — galaxies: nuclei — galaxies: Seyfert — galaxies: structure

## 1. INTRODUCTION

\* Based on observations with the NASA/ESA *Hubble Space Telescope*, obtained at the Space Telescope Science Institute, which is operated by AURA Inc, under NASA contract NAS 5-26555.

<sup>1</sup> Department of Astronomy and Astrophysics, 525 Davey Lab, The Pennsylvania State University, University Park, PA 16802, USA

<sup>2</sup> University of California Observatories/Lick Observatory and Department of Astronomy and Astrophysics, University of California, Santa Cruz, CA 95064, USA

<sup>3</sup> Irfu/Service d'Astrophysique, CEA-Saclay, Orme des Merisiers, 91191 Gif-sur-Yvette Cedex, France

<sup>4</sup> Steward Observatory, University of Arizona, 933 North Cherry Avenue, Tucson, AZ 85721, USA

<sup>5</sup> Space Telescope Science Institute, 3700 San Martin Drive, Baltimore, MD 21218, USA

<sup>6</sup> Department of Astronomy, University of Michigan, 500 Church St., Ann Arbor, MI 48109, USA

<sup>7</sup> Center for Astrophysics and Planetary Science, Racah Institute of Physics, The Hebrew University, Jerusalem 91904, Israel

<sup>8</sup> California Institute of Technology, MC 105-24, 1200 East California Boulevard, Pasadena, CA 91125 USA

<sup>9</sup> Department of Physics and Astronomy, University of Kentucky, Lexington, KY 40506, USA

<sup>10</sup> Department of Physics and Astronomy, University of Missouri-Kansas City, 5110 Rockhill Rd, Kansas City, MO 64110, USA

<sup>11</sup> Department of Astronomy, Yale University, New Haven, CT 06520, USA

<sup>12</sup> Max-Planck-Institut für Astronomie (MPIA), Königstuhl 17, D-69117 Heidelberg, Germany

<sup>13</sup> Max-Planck-Institut für extraterrestrische Physik (MPE), Giessenbachstrasse 1, D-85748 Garching bei München, Germany

<sup>†</sup> Hubble Fellow

The observed correlations between the mass of a supermassive black hole (SMBH) and the properties of its host galaxy bulge (e.g. Magorrian et al. 1998; Gültekin et al. 2009) imply that SMBH and bulge growth may be linked. To maintain the SMBH-bulge relations over a galaxy's long evolutionary history, rapid SMBH accretion in active galactic nucleus (AGN) phases probably coincide with periods of high star formation rate in the host galaxy. Indeed, rapidly accreting AGNs are observed to be predominantly located in the rapidly star-forming galaxies, from the local universe (Kauffmann et al. 2003b; Trump et al. 2013b) to higher redshifts (Mullaney et al. 2012; Harrison et al. 2012; Chen et al. 2013; Rosario et al. 2013a,b). But the detailed physical processes behind the coupled growth of SMBHs and galaxies remain mysterious.

A key difficulty for any AGN/galaxy coevolution model is in efficiently funneling gas down to the SMBH sphere of influence. Gas-rich major mergers of galaxies are an effective means to accomplish this, simultaneously (or near-simultaneously) igniting both a starburst and a luminous AGN (Sanders et al. 1988; Di Matteo, Springel, & Hernquist 2005; Hopkins et al. 2006). However many observations indicate that AGNs do not prefer merger remnant hosts (Grogin et al. 2005; Gabor et al. 2009; Cisternas et al. 2011; Kocevski et al. 2012), and major mergers are likely to fuel only nearby AGNs (Koss et al. 2010; Ellison et al. 2011) or the rare population of very luminous quasars (Trump 2011c; Treister et al. 2012).

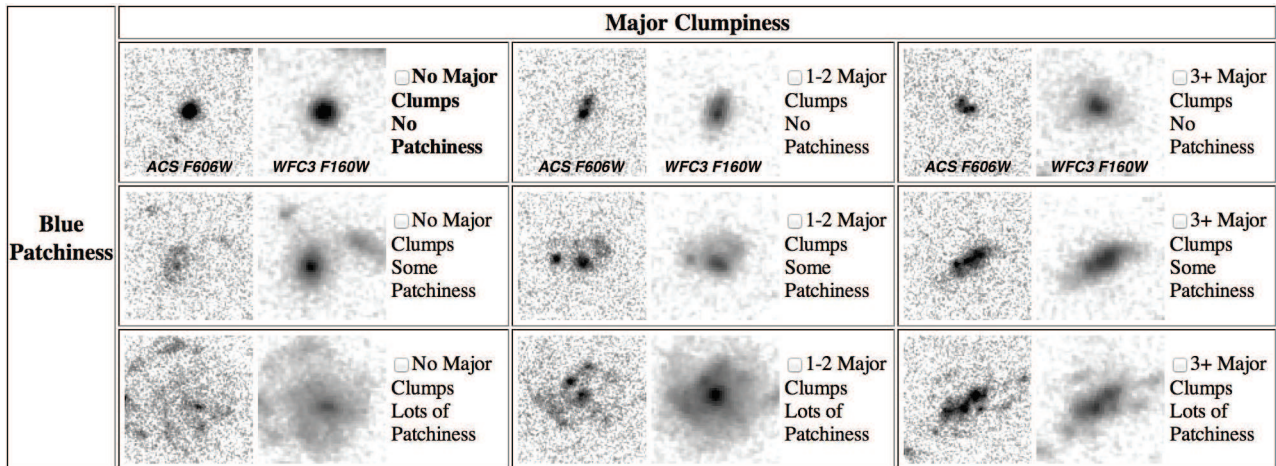


FIG. 1.— The diagram used for visual classification of clumpiness. The classification grid includes 9 template galaxies, each with images in the ACS F606W (rest-frame UV) and WFC3 F160W (rest-frame optical). For each galaxy in GOODS-S, classifiers chose the template galaxy which best matched in both bands (with a focus on the F606W, where clumps are most visible). We sum both axes and average over the 5 classifiers to assign each galaxy a “total clumpiness”  $C$  from 0 (top left) to 4 (bottom right), motivated by theoretical simulations which demonstrate that patchiness might simply be clumpiness reprocessed by dust. Clumpy galaxies have  $C \geq 2$ , smooth galaxies have  $C \leq 1$ , and intermediate galaxies have  $1 < C < 2$ .

Violent disk instabilities might provide another solution to the gas inflow problem (Bournaud et al. 2011). These models are supported by the observation that massive galaxies at  $z \sim 2$  frequently have most of their star formation in massive ( $10^8$ - $10^9 M_{\odot}$ , 100 – 500 pc) clumps within irregular galaxies (Cowie, Hu & Songaila 1995; Elmegreen, Elmegreen & Hirst 2004; Ravindranath et al. 2006; Guo et al. 2012), unlike the much smoother morphologies of similar-mass star-forming galaxies in the local universe. The kinematics of these clumps indicate that they are not accreted as minor mergers, but instead form as in-situ gravitational instabilities (Shapiro et al. 2008; Bournaud et al. 2008; Förster Schreiber et al. 2009; Genzel et al. 2011; Mandelker et al. 2014). The high gas fractions observed in  $z \sim 2$  galaxies (Tacconi et al. 2010; Daddi et al. 2010), likely accreted as cold gas along filaments of the cosmic web (Kereš et al. 2005; Dekel et al. 2006, 2009), would naturally result in highly turbulent star-forming clumps (Hernquist 1989; Shlosman & Noguchi 1993; Dekel, Sar & Ceverino 2009).

Violent disk instabilities might lead to clumps rapidly falling into the center of a galaxy and efficiently fueling a luminous AGN (Bournaud et al. 2011). This remains a point of debate, however, as most simulations lack the resolution and detailed physics to follow the gas all the way into a galaxy’s center. Observations indicate that star-forming clumps at  $z \sim 2$  typically make up only a small fraction of their galaxy’s stellar mass, suggesting that they may be too short-lived to migrate all the way into a galaxy center (Wuyts et al. 2012). Indeed, simulations show that clumps might be destroyed by feedback (Hopkins et al. 2012; Hopkins, Kereš & Murray 2013) or exhausted by star formation (Forbes et al. 2014) before reaching the nuclear AGN. On the other hand, other simulations find that clumps are sufficiently long-lived to form central bulges and fuel AGNs even with feedback and mass loss (Bournaud et al. 2014), and the gas between clumps, rather than the clumps themselves, may be more important for large-scale inflows anyway (e.g.

Dekel et al. 2013). In support of AGN fueling from violent disk instabilities, Bournaud et al. (2012) found direct observational evidence for a higher AGN fraction in a small sample (14) of  $z \sim 0.7$  clumpy galaxies compared to smooth (non-clumpy) extended disks matched in stellar mass and redshift.

Here we extend the search for a connection between clumps and AGNs to  $1.3 < z < 2.4$ , using data from the Cosmic Assembly Near-Infrared Legacy Survey (CANDELS Grogin et al. 2011; Koekemoer et al. 2011). This redshift range is particularly interesting because it represents the peak of both cosmic star formation and the AGN luminosity function (e.g. Hopkins & Beacom 2006; Aird et al. 2010). Cold gas inflows and resultant violent disk instabilities are also most prominent in simulations at  $z \sim 2$  (Kereš et al. 2005; Dekel, Sar & Ceverino 2009). And in contrast to the local universe, AGNs at  $z > 1$  may be unique in growing before a host galaxy bulge develops, with evidence from both evolution in BH-bulge relations (Peng et al. 2006; Jahnke et al. 2009; Bennert et al. 2011; Cisternas et al. 2011) and from stacked detection of AGN signatures in low-mass disk galaxies (Trump et al. 2011b; Xue et al. 2012). The gravitational torques provided by violent disk instabilities provide a potential way to fuel an AGN in a disk galaxy even while the bulge is still under construction.

Section 2 describes the combination of Hubble Space Telescope (*HST*) Wide Field Camera 3 (WFC3) near-infrared (IR) imaging and spectroscopy used to construct and study our samples of  $z \sim 2$  galaxies with clumpy, smooth, and intermediate morphologies. We identify AGNs using X-ray emission, emission-line diagnostics, and spatially resolved emission-line ratios: as Section 3 describes, this includes a broad range of AGN properties and avoids contamination by shock-dominated galaxies. We put these selection techniques together in Section 4, and demonstrate that clumpy galaxies are not more likely to host AGNs than smoother galaxies. Section 5 concludes with a discussion of what these results mean for AGN/galaxy coevolution at  $z \sim 2$ . Throughout the pa-

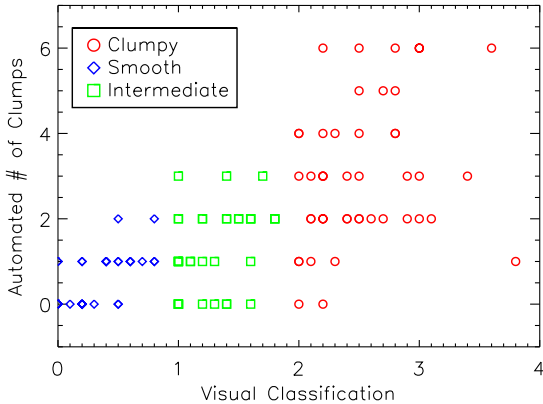


FIG. 2.— Comparison between the automated number of clumps from Guo et al. (2014) and the visual clumpiness used in this work. There is a loose correlation between the two measures of clumpiness, matching the  $\sim 75\%$  agreement between automated and visual methods found by Guo et al. (2014).

per we use a standard  $\Lambda$ CDM cosmology with  $h_0 = 0.7$ .

## 2. OBSERVATIONAL DATA

We select a sample of 44 clumpy galaxies from the Great Observatories Origins Deep Survey South (GOODS-S Giavalisco et al. 2004) region of CANDELS. For comparison, we also construct mass-matched samples of 41 smooth (non-clumpy) and 35 intermediate galaxies. All galaxies have  $H < 24$  (to ensure reliable classification of clumpiness) and have [OIII] detected at the  $3\sigma$  level (for reliable AGN line ratio diagnostics) in the redshift range  $1.3 < z < 2.4$ . The effective limits on star formation rate (SFR) and stellar mass ( $M_*$ ) caused by these flux limits are discussed in Section 2.3. Each morphology category has a median redshift of  $z = 1.85$ . Redshifts and emission line measurements come from *HST*/WFC3 grism spectroscopy taken by the 3D-*HST* survey (Brammer et al. 2012).

The observational data are described below, with particular attention to the methods for clumpiness classification and AGN identification. The derived data for the clumpy, smooth, and intermediate galaxies are presented in Table 1.

### 2.1. Visual Morphologies: Clumpy, Smooth, and Intermediate

Our samples of clumpy, smooth, and intermediate galaxies come from the 4-epoch CANDELS GOODS-S visual classification catalog (Kartaltepe et al. 2014). Each galaxy has high-resolution *HST* imaging in the rest-frame UV from ACS F606W and F850LP and in the rest-frame optical from WFC3 F125W and F160W (Grogin et al. 2011; Koekemoer et al. 2011). Galaxies were classified on the clumpiness/patchiness grid shown in Figure 1. Here “clumpiness” is a measure of the number of compact knots, while “patchiness” refers to the more diffuse irregularities within galaxies.

We use visual classification because automated selection of clumps and patchiness remains a difficult computational problem (e.g. Guo et al. 2012). Inspectors were instructed to focus on the bluest passband for clumpiness classification, as clumps are typically most evident in in the rest-UV (Guo et al. 2012). All galaxies in our sample

(from the 4-epoch catalog of Kartaltepe et al. 2014) were inspected by at least five classifiers, and we combine the different classifications into a single averaged result for each galaxy.

We use both clumpiness and patchiness as indicators of violent disk instabilities within a galaxy. This is motivated by the presence of both compact/round clumps and diffuse/elongated structures in simulations of  $z \sim 2$  galaxies undergoing violent disk instabilities (Ceverino et al. 2012; Mandelker et al. 2014). In addition, if star-forming clumps are enshrouded by dust, their emission would likely be reprocessed in a patchy morphology. Observations show that galaxies appearing clumpy in the UV are merely patchy morphologies in the near-infrared: adding dust to such a system would cause it to appear patchy in the UV rather than clumpy. We also note that Guo et al. (2014) find better agreement between automated clump-finding and visual classification when patchiness is included in the visual clumpiness. Therefore we combine both axes in Figure 1 for the identification of clumpy galaxies.

The classifications on each axis are summed to give each galaxy a clumpiness+patchiness value ranging from 0 to 4. Here 0 represents the top left (no clumpiness, no patchiness) and 4 represents the lower right (3+ clumps and maximally patchy). The individual classification results are averaged together to assign “total clumpiness” parameter  $C$ , which we use to define the galaxies most and least likely to be dominated by violent disk instabilities. We define  $C \geq 2$  galaxies as “clumpy,”  $C < 1$  galaxies as “smooth,” and  $1 \leq C < 2$  galaxies as “intermediate.” These divisions are chosen such that each category has roughly the same number of galaxies, for ease of comparing AGN fractions across morphologies.

We compare the visual classification  $C$  with the automated number of clumps from (Guo et al. 2014) in Figure 2. There is a loose correlation between the two methods: the visually-identified smooth galaxies tend to have the fewest automated number of clumps, while the visually clumpy galaxies typically have the most automated number of clumps. There is some scatter due to the imperfection of both methods. Guo et al. (2014) include a more detailed comparison of automated clump-finding with the same visual classifications used here, finding  $\sim 75\%$  agreement between the two methods (see their Appendix).

Figure 3 shows *HST*  $iJH$  (rest UV-optical) color composite images for several representative clumpy, smooth, and intermediate galaxies in our sample. Images of all galaxies are additionally shown in the Appendix (Figures 15, 16, and 17).

### 2.2. *HST*/WFC3 G141 Slitless Grism

The GOODS-S region of CANDELS has near-complete spectroscopic coverage in the near-IR from publicly available 2-orbit *HST*/WFC3 G141 grism observations taken by the 3D-*HST* survey (Brammer et al. 2012). For redshifts and line measurements of individual galaxies, the data were reduced using the *axE* software (Kümmel et al. 2009, available at <http://axe.stsci.edu/axe/>) to produce 2D and 1D wavelength- and flux-calibrated spectra at  $1.1 < \lambda < 1.7\mu\text{m}$ . We used the *specpro* IDL

TABLE 1  
 GALAXY PROPERTIES

ID	Morphology	RA	Dec	$z$	$f(\text{H}\beta)$	$f([\text{OIII}])$	$\log(M_*)$
-	-	(deg)	(J2000)	-	$10^{-18}$ erg s $^{-1}$ cm $^{-2}$	$10^{-18}$ erg s $^{-1}$ cm $^{-2}$	( $\log(M_\odot)$ )
7502	clumpy	53.07221603	-27.84033012	1.61	$99.95 \pm 28.56$	$83.47 \pm 24.51$	9.63
7897	clumpy	53.14831924	-27.83686638	1.90	$23.49 \pm 12.22$	$27.09 \pm 8.42$	9.82
7907	clumpy	53.15573502	-27.83712769	1.39	$18.95 \pm 13.73$	$169.79 \pm 21.69$	9.67
7930	clumpy	53.15451050	-27.83648491	2.03	$14.20 \pm 10.43$	$43.64 \pm 10.26$	9.41
8206 <sup>a</sup>	clumpy	53.14358902	-27.83471107	1.99	$10.82 \pm 5.73$	$39.97 \pm 10.54$	9.85
5023	smooth	53.10656738	-27.86481476	1.90	< 3.31	$18.62 \pm 5.92$	9.74
5728	smooth	53.08922577	-27.85734558	2.03	$16.80 \pm 7.95$	$79.73 \pm 11.31$	10.37
6278 <sup>b</sup>	smooth	53.06018448	-27.85304642	1.54	< 2.73	$240.61 \pm 21.63$	10.79
6678	smooth	53.07507324	-27.84802055	1.73	$37.84 \pm 7.38$	$21.91 \pm 6.77$	10.14
7806	smooth	53.16970062	-27.83803558	1.94	$8.18 \pm 7.71$	$38.97 \pm 11.10$	10.37
5552	intermed	53.06779480	-27.85925293	1.55	$15.67 \pm 14.78$	$73.40 \pm 16.57$	9.81
6895	intermed	53.09495926	-27.84582710	1.56	< 4.50	$49.29 \pm 8.75$	9.44
7952	intermed	53.18961334	-27.83626175	2.09	$39.79 \pm 13.92$	$52.87 \pm 9.57$	9.89
8124	intermed	53.10293198	-27.83484268	1.38	$55.60 \pm 21.62$	$102.88 \pm 15.12$	9.18
8307	intermed	53.07443237	-27.83325577	1.54	< 6.95	$55.32 \pm 10.17$	9.26

NOTE. — Weak  $\text{H}\beta$  lines detected below a  $1\sigma$  threshold are treated as upper limits (using the  $1\sigma$  error as the limit). The full catalog of 44 clumpy galaxies, 41 smooth galaxies, and 35 intermediate galaxies appears as a machine-readable table in the electronic version.

<sup>a</sup> X-ray detected, but in the soft band only and consistent with emission from a star-forming galaxy (Xue et al. 2011).

<sup>b</sup> X-ray detected and classified as an AGN by Xue et al. (2011).

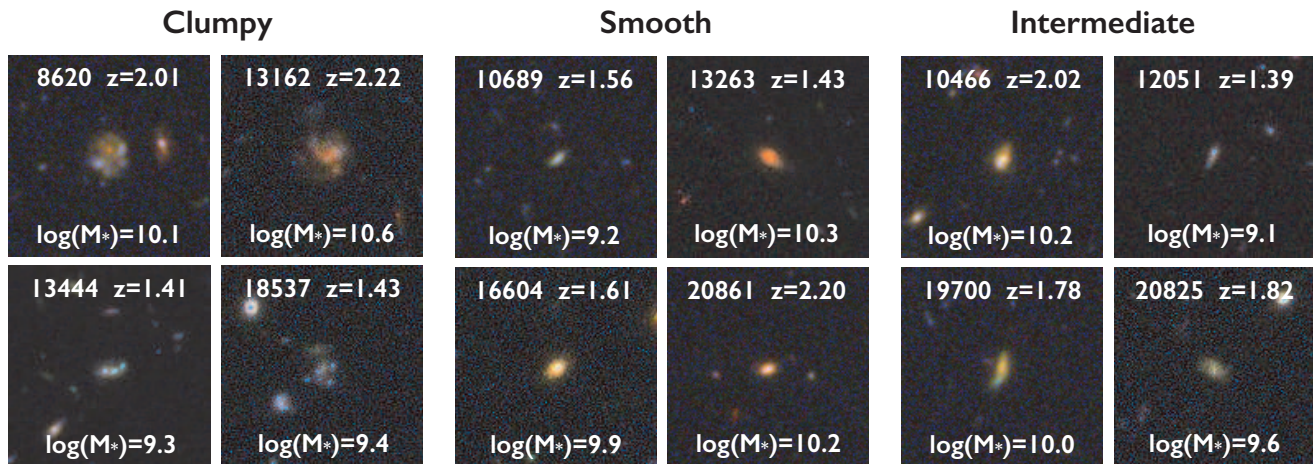


FIG. 3.— Images of four clumpy, four smooth, and four intermediate-morphology galaxies, chosen to be representative in redshift and stellar mass (stellar masses given in each panel are in units of solar mass). Each thumbnail is  $10''$  on a side and is a color-composite using the *HST*/ACS  $i$  and WFC3  $JH$  band observations.

software<sup>16</sup> (Masters & Capak 2011) to visually inspect and determine cross-correlation redshifts for the samples of clumpy, smooth, and intermediate galaxies. Spectra with significant ( $>10\%$ ) contamination (from neighboring objects) in the  $\text{H}\beta$ + $[\text{OIII}]$  region are rejected from each sample: this occurs for about  $\sim 15\%$  of galaxies.

Line fluxes and ratios of  $\text{H}\beta$  and  $[\text{OIII}]\lambda 5007\text{\AA}$  were also measured from the aXe-reduced 3D-HST spectra. The low resolution of the WFC3 slitless grism ( $R \simeq 130$  and  $46.5\text{\AA}/\text{pixel}$ , worse for extended sources) means that the  $\text{H}\beta$  and  $[\text{OIII}]\lambda 4959, 5007\text{\AA}$  lines are somewhat blended. We simultaneously fit all three lines with Gaussians, constraining each line to be fit within (rest-frame)  $50\text{\AA}$  ( $\sim 2$ - $3$  pixels) of the line center. We do not constrain the width of each line because the spatial broadening of the slitless grism frequently causes unusual profiles which can dif-

fer for each line. The  $\text{H}\beta$  line flux is measured directly from the Gaussian fit, while the  $[\text{OIII}]\lambda 5007$  flux is measured as  $3/4$  of the total flux from both blended  $[\text{OIII}]$  Gaussians (Storey & Zeppen 2000). If we instead fix the two  $[\text{OIII}]$  Gaussians to have total fluxes with a 1:3 ratio, the measured line fluxes do not significantly change. Examples of the line fits are shown in Figure 4.

Uncertainties in the line ratios are computed by re-fitting continua and Gaussians on 10000 realizations of the resampled data. Our sample includes only galaxies with  $[\text{OIII}]\lambda 5007\text{\AA}$  fluxes measured at the  $3\sigma$  level. We do not set any requirement on the  $\text{H}\beta$  line flux measurements, and  $\text{H}\beta$  line fluxes less than the  $1\sigma$  error are treated as upper limits (using the  $1\sigma$  error as the limit). In general, the unique asymmetric shape of the blended  $[\text{OIII}]$  lines enables secure redshifts even when  $\text{H}\beta$  is poorly detected.

To study spatially resolved line ratios, we used separate reductions of the WFC3 G141 data from the 3D-HST

<sup>16</sup> The specpro package is available at <http://specpro.caltech.edu>

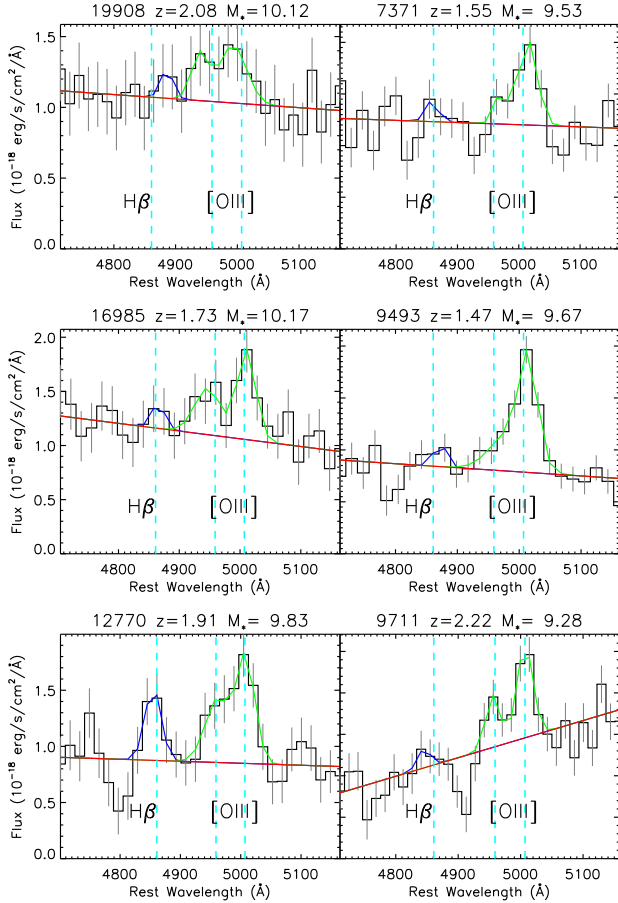


FIG. 4.— Example line fits to the  $H\beta + [OIII]$  regions. The blended lines are simultaneously fit by three Gaussians, with the  $H\beta$  flux measured directly from the  $H\beta$  Gaussian fit, and the  $[OIII]\lambda 5007$  line computed as 3/4 of the two  $[OIII]$  Gaussians. The top row shows spectra of two clumpy galaxies, the middle row is smooth galaxies, and the bottom row is intermediate galaxies. Both 19908 and 16985 have weak  $H\beta$  emission detected below  $1\sigma$  significance, and for these galaxies the  $1\sigma$  errors in  $H\beta$  are treated as upper limits.

pipeline, as described in Brammer et al. (2012, 2013). The 3D-HST reduction method produces superior spatially resolved spectra because it interlaces rather than drizzles: this mitigates the correlated noise associated with drizzling in the final high-resolution ( $0''.06/\text{pixel}$ ) combined 2D spectra.

### 2.3. Stellar Masses and Star Formation Rates

We calculate stellar masses and star formation rates for the clumpy, smooth, and intermediate galaxies using the extensive UV / optical / IR photometry in GOODS-S, with 18 bands including 8 with high-resolution *HST* imaging (Guo et al. 2013). First, the spectroscopic redshift from the *HST*/WFC3 grism is used to shift the observed photometry to the rest-frame. We then fit the rest-frame spectral energy distribution (SED) with Bruzual & Charlot (2003) models that include a Chabrier (2003) initial mass function, exponentially declining star-formation histories, and a Calzetti (2001) extinction law. Stellar mass is given by the best-fit model. Example SED fits (for the same galaxies shown in Figure 4) are shown in Figure 5.

There is some evidence that  $z \sim 2$  galaxies are more

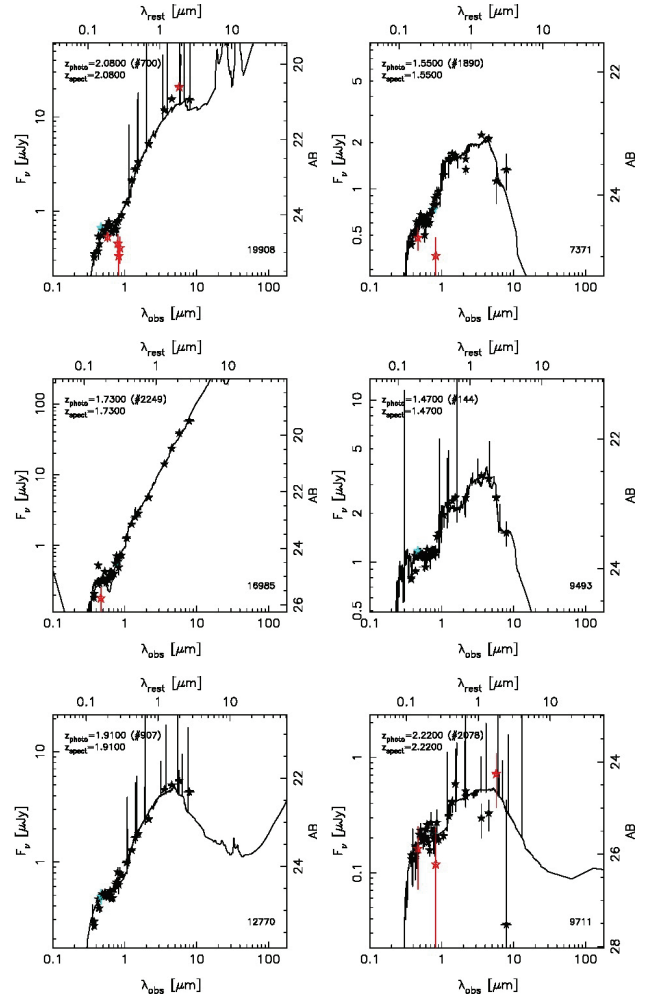


FIG. 5.— Best-fit models to the SEDs of the same galaxies shown in Figure 4. Stellar masses are computed from these best-fit Bruzual & Charlot (2003) models. The SED of the galaxy 16985 (which is an X-ray AGN) has red near-IR colors suggestive of an AGN (e.g. Donley et al. 2012): it is the only galaxy in the sample which might have significant AGN contribution to the SED.

likely to have constant star-formation histories rather than the exponentially declining models used here. In practice, our best-fit SEDs generally have  $\tau$  values which are very long (parameterizing the star formation history as  $SFR \sim e^{-t/\tau}$ ). We also tested the effects of forcing a constant star formation history, and found the masses to change by only  $\lesssim 0.1$  dex in all cases.

Meanwhile star formation rates (SFRs) are calculated following the method of Wuyts et al. (2011) when mid- and far-IR data are available, and SED-fitting following the method of Barro et al. (2013) otherwise. IR emission from an intrinsically luminous AGN might contaminate the IR with a hot dust bump (effectively observed as red IRAC colors, e.g. Donley et al. 2012), influencing both the stellar mass and SFR estimates. This occurs for one of our objects: the clumpy galaxy and X-ray AGN 16985, shown in Figure 5. The remainder of the sample have well-fit galaxy SEDs without evidence for significant AGN contribution. This is unsurprising, as only intrinsically luminous ( $\log(L_X) \gtrsim 44$ ) AGNs tend to have hot dust IR emission which dominates over the galaxy emission (Trump et al. 2011a; Donley et al. 2012).

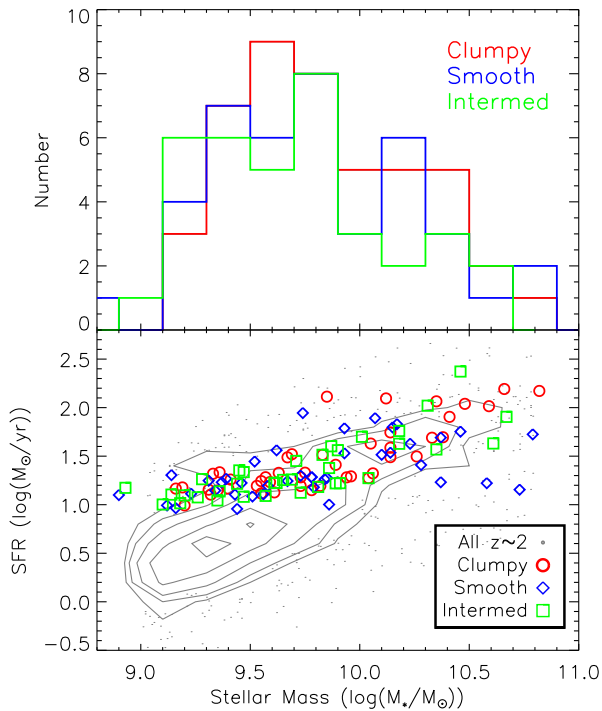


FIG. 6.— *Top*: Histograms showing stellar mass distribution for each sample. The smooth and intermediate galaxies are chosen to have the same mass distribution as the clumpy galaxies. *Bottom*: Star formation rate vs. stellar mass for the clumpy, smooth, and intermediate galaxies studied in this work (colored points). The contours show the larger population of galaxies with  $1.3 < z_{\text{phot}} < 2.4$  in the same GOODS-S region. While the SFR is estimated from the Wuyts et al. (2011) UV+IR method, it is correlated with the [OIII] emission line flux, and the observed  $\text{SFR} \gtrsim 10 M_{\odot} \text{ yr}^{-1}$  limit is a consequence of the  $3\sigma$  [OIII] detection limit. Meanwhile the  $H < 24$  selection causes the  $M_{*} \gtrsim 10^9 M_{\odot}$  limit.

Figure 6 (top panel) shows the mass distributions for each of the clumpy, smooth, and intermediate galaxy samples. The three samples are selected to be matched in stellar mass: starting with the clumpy galaxy sample, we constructed the smooth and intermediate galaxy samples to have a similar mass distribution. All three samples have median and mean  $M_{*} = 10^{9.8} M_{\odot}$ .

Our galaxies are plotted in  $\text{SFR} - M_{*}$  space in Figure 6 (bottom panel). For comparison we also show the SFR and  $M_{*}$  of the larger population of GOODS-S galaxies with photometric redshifts calculated by Dahlen et al. (2013) in the same  $1.3 < z < 2.4$  redshift range. Our  $z \sim 1.85$  galaxies are limited to  $M_{*} \gtrsim 10^9 M_{\odot}$  by the  $H < 24$  selection criterion. The requirement for [OIII] detection at the  $3\sigma$  level imposes a flux limit of  $f([\text{OIII}]) \gtrsim 5 \times 10^{-17} \text{ erg s}^{-1} \text{ cm}^{-2}$  in the 2-orbit WFC3 grism data. Although we estimate SFR from the SED (following Wuyts et al. 2011) rather than from emission lines, this [OIII] line flux translates roughly to the observed SFR limit of  $\text{SFR} \gtrsim 10 M_{\odot} \text{ yr}^{-1}$  (assuming  $f(\text{H}\alpha) \sim f([\text{OIII}])$  and using the Kennicutt 1998 relation). For the lower-mass half of the sample ( $M_{*} < 10^{9.8} M_{\odot}$ ), this SFR limit restricts the galaxies to be starbursting and above the star-forming “main sequence” (see also Noeske et al. 2007; Daddi et al. 2007). On the other hand the higher-mass half of the sample ( $M_{*} > 10^{9.8} M_{\odot}$ ) generally lies on the main sequence for star-forming galaxies at  $1.3 < z < 2.4$ . The only notable

exception is a few high-mass smooth galaxies below the main sequence which might be quenching.

#### 2.4. X-ray Data

The CANDELS GOODS-S field also contains 4 Ms of *Chandra* X-ray data (Xue et al. 2011). The 4 Ms depth corresponds to an on-axis flux limit of  $3.2 \times 10^{-17} \text{ erg s}^{-1} \text{ cm}^{-2}$ , which corresponds to a luminosity limit of  $L_X > 10^{41.9} \text{ erg s}^{-1}$  at our sample’s median redshift of  $z = 1.85$ . We use the classifications of Xue et al. (2011) to separate X-ray galaxies (with X-ray detections consistent with the  $L_X - \text{SFR}$  relation, Lehmer et al. 2010; Mineo et al. 2014) from the more luminous and hard-spectrum AGNs. The X-ray data for undetected sources in each morphology category are also stacked, as discussed in Section 3.3.

### 3. AGNS IN CLUMPY GALAXIES?

We compare the AGN fraction of clumpy galaxies with the AGN fraction among the mass-matched smooth and intermediate galaxies. AGN detection is accomplished in three different ways: with standard line ratio selection via the “mass-excitation” method (Juneau et al. 2011), with spatially resolved line ratios, and with X-rays (both for individual sources and stacks of each morphological category).

#### 3.1. Mass Excitation Diagnostic for AGNs

It has long been known that the high-ionization emission of AGNs results in a different emission line signature than observed in typical HII regions associated with star formation (SF): in particular, AGN narrow line regions tend to exhibit higher ratios of collisionally excited “forbidden” lines to hydrogen recombination lines (Seyfert 1943; Osterbrock & Parker 1965). The classic Baldwin, Phillips & Terlevich (1981, BPT) and Veilleux & Osterbrock (1987, VO87) AGN/SF diagnostics use the ratios of  $f([\text{OIII}]\lambda 5007)/f(\text{H}\beta)$  vs.  $f([\text{NII}]\lambda 6584)/f(\text{H}\alpha)$  or  $f([\text{SII}]\lambda 6718+6731)/f(\text{H}\alpha)$ : the small wavelength separation of each line pair means that these ratios are effectively insensitive to reddening.

The low resolution of the WFC3 grism means that the [NII] and H $\alpha$  lines are not resolved from one another, and so the standard BPT or VO87 diagnostics cannot be used on our data. Instead we use the “mass-excitation” (MEX) method (Juneau et al. 2011), which uses the [OIII]/H $\beta$  ratio with the stellar mass  $M_{*}$  to separate AGN and SF galaxies. Functionally, the MEX method uses the correlation between mass and metallicity (e.g. Tremonti et al. 2004) to separate low-metallicity galaxies from AGN, both of which exhibit similarly high [OIII]/H $\beta$  ratios. Compared to X-ray or infrared surveys, line ratio selection is often more sensitive to obscured and moderately accreting AGN, but it also less reliable (e.g. Juneau et al. 2014). There is also some debate whether line ratio diagnostics remain applicable in  $z > 1$  galaxies at all, since higher redshift galaxies may have different gas properties (Liu et al. 2008; Brinchmann, Pettini & Charlot 2008; Kewley et al. 2013), changing their line ratios in the absence of AGN (but for counterarguments, see Wright et al. 2010; Trump et al. 2011b, 2013a). Juneau et al. (2014) also demonstrate that the different selection effects in high- and low-redshift samples have

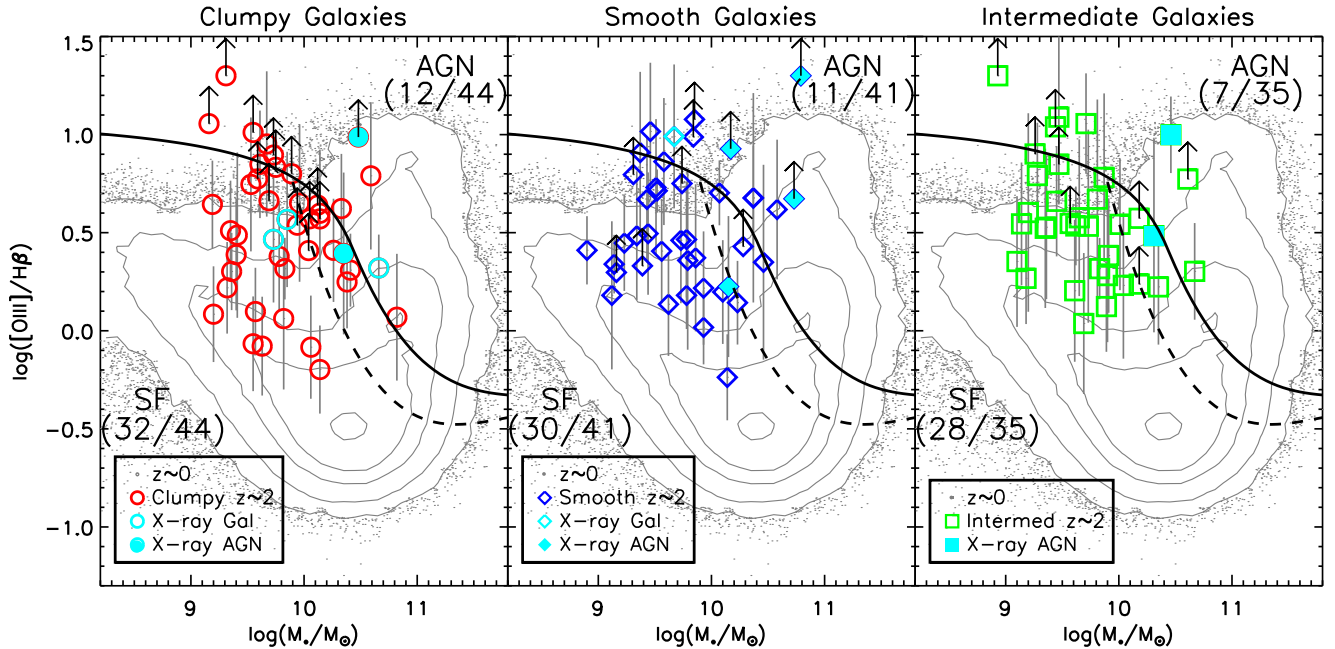


FIG. 7.— The mass-excitation (MEx) diagnostic (Juneau et al. 2011) of  $[\text{OIII}]/\text{H}\beta$  line ratio versus stellar mass. Panels from left to right show clumpy galaxies, smooth galaxies, and intermediate-morphology galaxies. Cyan symbols indicate galaxies detected in X-rays: filled symbols are X-ray AGN, while open cyan symbols are consistent with X-ray galaxies (i.e., with X-rays powered by non-AGN processes). For comparison, each panel also shows a  $z \sim 0$  galaxy sample from the SDSS. The fraction of MEx AGN is slightly higher for the clumpy galaxies (29% AGN) than for the samples of smooth (27% AGN) and intermediate (20% AGN) galaxies. However we show in Sections 3.2 and 3.3 that this is likely due to extended high-ionization phenomena (e.g., clumpy star formation) rather than nuclear AGN.

important effects on their observed MEx distributions. For this reason we avoid comparing the  $z \sim 1.5$  galaxy samples with local objects. Instead we simply compare clumpy, smooth, and intermediate galaxies all within the same redshift range.

Figure 7 shows the MEx diagram for the clumpy, smooth, and intermediate galaxies. The solid line in each panel shows the empirical line from Juneau et al. (2014) dividing AGN and SF galaxies, adjusted for the redshift ( $z \sim 1.85$ ) and line flux limit ( $f([\text{OIII}]) \gtrsim 5 \times 10^{-17} \text{ erg s}^{-1} \text{ cm}^{-2}$ ):

$$y = 0.375/(m - 10.4) + 1.14 \text{ if } m \leq 9.88 \quad (1)$$

$$y = 290.2 - 76.34m + 6.69m^2 - 0.1955m^3 \text{ otherwise.} \quad (2)$$

Here  $y = \log([\text{OIII}]/\text{H}\beta)$  and  $m = \log(M_*/M_\odot) - 0.51$ . Assuming that all galaxies above this line are AGNs, clumpy galaxies seem to have the highest AGN fraction (12/44, 27%), followed by smooth galaxies (11/41, 27%) and intermediate galaxies (7/35, 20%).

However the simple binary classification of counting objects above and below the AGN/SF line is not entirely appropriate, given that most galaxies have emission lines with composite contribution from both SMBH accretion and HII regions. The MEx diagram is much more suited to a probabilistic classification approach, as introduced by Juneau et al. (2011). The MEx probabilities, updated for use at  $z > 1$  by Juneau et al. (2014) and assuming an error of 0.2 dex in  $M_*$ , indicate that  $39^{+8}_{-6}\%$  of clumpy,  $36^{+8}_{-6}\%$  of smooth, and  $35^{+9}_{-7}\%$  of intermediate galaxies are AGN-dominated. Given the uncertainty of the MEx diagram at  $z > 1$  (e.g. Kewley et al. 2013; Newman et al. 2014; Juneau et al. 2014), these probabilities do not necessarily represent absolute AGN fractions,

but they remain useful for comparing relative AGN fractions among the three morphology classes. The three AGN fractions are all consistent with one another, and the clumpy galaxies have only marginally ( $<1\sigma$ ) more AGNs than smoother galaxies. In the next two subsections we show that the higher line ratios in clumpy galaxies are likely an effect of high ionization in extended regions (due to shocks or dense star-forming clumps) rather than nuclear AGN.

### 3.2. Spatially Resolved Line Ratios

The traditional BPT and MEx methods use line ratios integrated over the entire galaxy, and thus may be diluted by star formation and/or affected by non-nuclear ionization that has nothing to do with AGN activity. In particular, the violent disk instabilities of clumpy galaxies may lead to high-velocity shocks or dense HII regions which can mimic AGN-like line ratios (e.g. Rich, Kewley & Dopita 2011; Newman et al. 2014). For this reason we use the spatial resolution of the WFC3 grism spectroscopy to go beyond integrated line ratios and investigate line ratio gradients, following Wright et al. (2010); Trump et al. (2011b). Spatially resolved line ratios can reveal if AGNs selected by integrated line ratios are the product of nuclear AGNs or extended phenomena (like shocks or high-ionization star formation).

The two-dimensional (2D) spectra of individual sources generally lack the signal-to-noise for well-measured spatially resolved line ratios, so we stack spectra of galaxies in each of the clumpy, smooth, and intermediate galaxy samples. Two stacks are constructed for each morphology class: one with all galaxies, and another using only galaxies classified as AGNs on the MEx diagram in Sec-

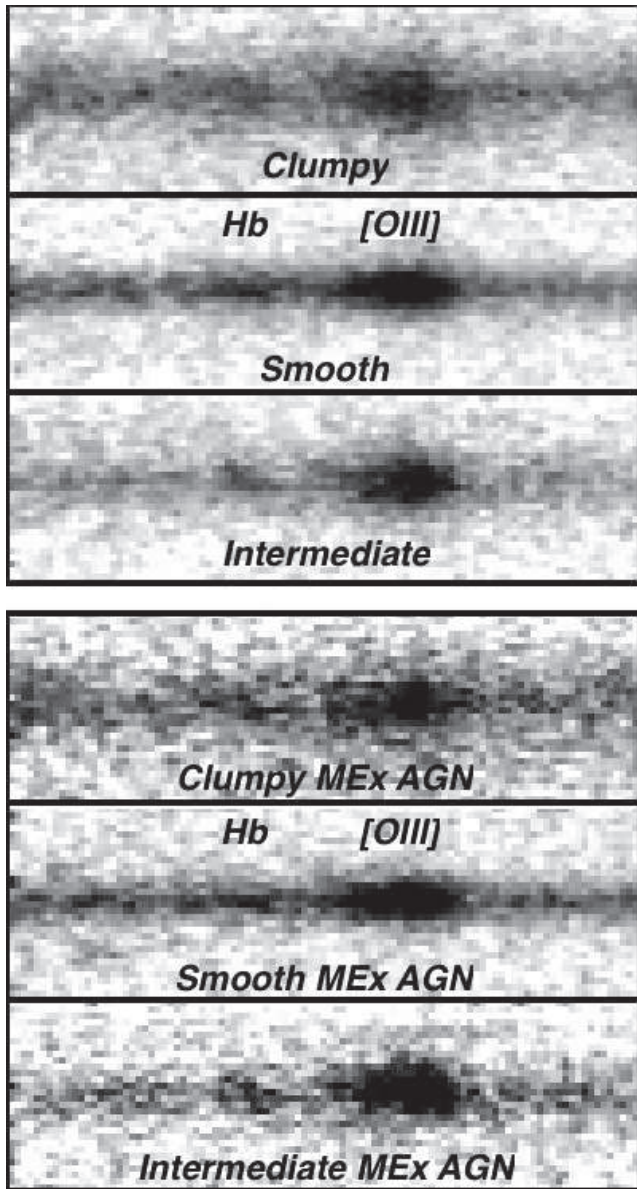


FIG. 8.— Stacked two-dimensional *HST*/WFC3 grism spectra for clumpy, smooth, and intermediate-morphology galaxies. The top three spectra are stacks of all galaxies in each morphology class, while the bottom three are stacks of MEx AGNs only. The emission line sizes in both the dispersion and cross-dispersion directions are a result of galaxy size rather than velocity due to the low resolution ( $R \sim 300$ ) of the slitless grism. The stacked data provide sufficient signal-to-noise to separately extract nuclear and extended one-dimensional spectra and line ratios.

tion 3.1. Centers of galaxies are defined by the SExtractor (Bertin & Arnouts 1996) coordinates in the F160W detection image, translated to a spectral trace in the dispersed G141 2D spectrum using well-calibrated polynomials from aXe which are typically accurate to  $\lesssim 0.2$  pixels. The image centroid and resultant spectral trace may not coincide with the brightest (continuum or emission line) flux of a galaxy, particularly for clumpy galaxies: we investigate centering on the brightest flux rather than image centroids in Section 4.1. Each galaxy spectrum is also normalized by its total [OIII] flux so that the stack is equal-weighted and not dominated by the most [OIII]-luminous AGNs. (This normalization means that the

TABLE 2  
STACKED SPECTRA NUCLEAR AND EXTENDED  
 $\log([\text{OIII}]/\text{H}\beta)$

Stack	Nuclear	Extended
All Clumpy	$3.5 \pm 0.8$	$4.5 \pm 1.2$
All Smooth	$3.2 \pm 0.4$	$2.6 \pm 1.2$
All Intermediate	$3.9 \pm 1.1$	$3.3 \pm 1.3$
MEx AGN Clumpy	$7.5 \pm 1.5$	$7.1 \pm 2.0$
MEx AGN Smooth	$8.3 \pm 1.4$	$5.8 \pm 1.3$
MEx AGN Intermediate	$11.8 \pm 2.1$	$9.8 \pm 2.3$
[OIII]-centered Clumpy AGNs	$5.5 \pm 1.2$	$10.5 \pm 1.8$

stacked line ratios are slightly lower than the mean of the individual ratios.) The stacked 2D spectra of all galaxies in each morphology class are shown in Figure 8. It is immediately evident that the clumpy galaxies are typically larger than the intermediate or smooth galaxies: for a galaxy to be classified as clumpy, it must be large enough for the clumps to be resolved in the *HST* data. Still, the smooth and intermediate galaxies are not so small as to be unresolved, and they have enough signal beyond the central three pixels to have well-measured extended (non-nuclear) spectra. We return to a discussion of the different sizes of the clumpy and smooth galaxies in Section 4.2.

We separately extract nuclear and extended one-dimensional (1D) spectra from the stacked data, shown in Figure 9. Here “nuclear” is defined as the central 3 pixels, corresponding to  $0''.18$  across and a  $\sim 1$  kpc radius at  $1.3 < z < 2.4$ . The “extended” spectra are extracted from pixels 3-6 on either side of the trace, translating to an annulus extending radially from  $\sim 2$ -4 kpc. It is possible that some emission from the AGN narrow line region extends into the extended aperture (Hainline et al. 2013; van der Laan et al. 2013), and the  $\sim 1$  kpc nuclear region is also likely to include some galaxy starlight. Although our regions will not perfectly disentangle AGN and galaxy light, the nuclear region preferentially includes AGN light and the extended region includes more galaxy starlight. Thus the spatially resolved line ratios are likely to be significantly more sensitive than the integrated line ratios.

The [OIII] and  $\text{H}\beta$  emission lines are measured from each nuclear and extended spectrum following the same method as in Section 2.2: three Gaussians were simultaneously fit to the continuum-subtracted spectra, with the [OIII] $\lambda 5007$  flux given as  $3/4$  of the total [OIII] $\lambda 4959+5007$  emission. Figure 10 shows the nuclear and extended [OIII]/ $\text{H}\beta$  ratios for the stacks of all clumpy, smooth, and intermediate galaxies in the MEx diagram (using the median stellar mass of each sample with small offsets between the points). Figure 11 shows the nuclear and extended line ratios using the stacked spectra of MEx AGN only. The nuclear and extended line ratio measurements for each stack are also presented in Table 2.

In the stacks of all galaxies in Figure 10, the nuclear and extended spectra are nearly indistinguishable. This indicates that there is not a dominant AGN population in any of the morphology classes. Nuclear AGNs begin to marginally emerge in Figure 11 in the stacked spectra of MEx AGNs among smooth galaxies. This implies that AGN classification using the up-

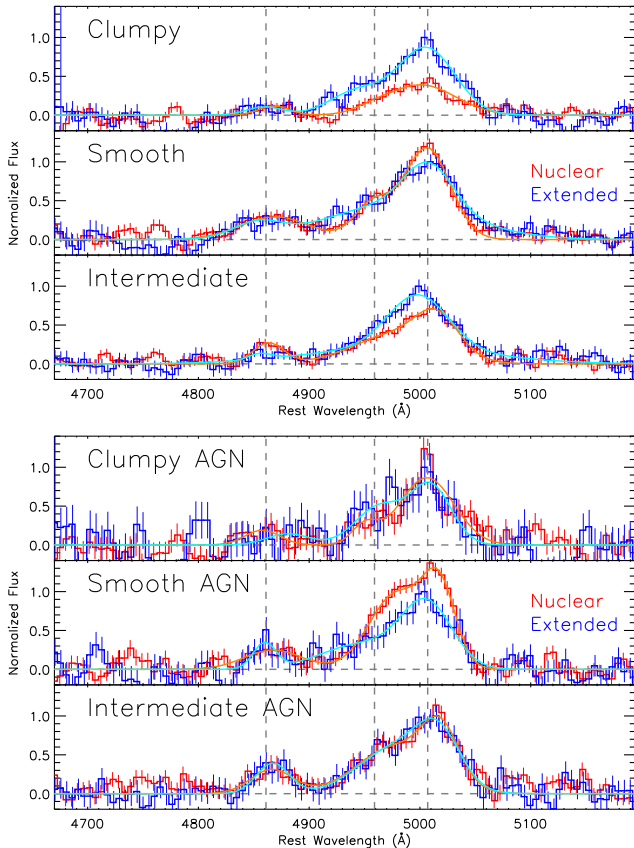


FIG. 9.— Nuclear and extended 1D spectra from the stacked *HST*/WFC3 grism data for clumpy, smooth, and intermediate-morphology galaxies. The top three panels are the stacked spectra of all galaxies, while the bottom three are for galaxies classified as MEx AGNs. The  $H\beta$  and  $[OIII]$  line centers are shown by the dashed lines, and the orange and cyan lines give the best-fit Gaussians to the nuclear and extended 1D spectra.

dated Juneau et al. (2014) MEx method is effective for smooth galaxies at  $z \sim 2$ , with their stacked spectra indicating nuclear AGN. The clumpy galaxies classified as MEx AGN, however, have essentially no difference in nuclear and extended  $[OIII]/H\beta$  ratios. The high  $[OIII]/H\beta$  ratios observed in the integrated spectra of clumpy galaxies are probably caused by extended phenomena like shocks or high-ionization star formation, both of which are likely in dense star forming clumps (Kewley et al. 2013; Newman et al. 2014; Rich, Kewley & Dopita 2014). Spatial line ratios indicate that clumpy galaxies may actually be *less* likely to host nuclear AGNs than smooth or intermediate galaxies. We further investigate the possibility of off-nuclear AGNs in Section 4.1.

### 3.3. X-ray AGN

X-rays tend to be the most efficient and least contaminated indicator of AGN activity, and so we also use the X-ray data to quantify the AGN fraction among clumpy, smooth, and intermediate morphology galaxies. All galaxies are matched to the Xue et al. (2011) 4 Ms *Chandra* catalog. In total, 5/44 clumpy, 4/41 smooth, and 2/35 intermediate galaxies have X-ray counterparts. X-ray detection is not sufficient for AGN classification, however, as luminous starburst ( $SFR \sim 300 M_{\odot}/yr$ ) galaxies can have enough X-ray binaries to exceed an

integrated luminosity of  $L_X \sim 10^{42}$  (Lehmer et al. 2010; Mineo et al. 2014). Xue et al. (2011) classify the GOODS-S X-ray sources into galaxies consistent with pure star formation or systems likely to be AGN on the basis of their spectral shape, X-ray to optical flux ratio, and X-ray luminosity. These classifications reveal that 2/48 clumpy, 3/41 smooth, and 2/35 intermediate galaxies are likely to be X-ray AGNs. The detection fractions and full-band luminosities of the X-ray AGNs are broadly consistent across the morphology categories, ranging from  $10^{42} - 10^{44}$  erg  $s^{-1}$ . X-ray data for the detected galaxies, as well as for the stacked non-detections (discussed below), are presented in Table 3.

Figure 12 presents the  $L_X - SFR$  relationship for X-ray detected sources, for both hard-band (2–8 keV) and soft-band (0.5–2 keV) luminosities. Also shown is the  $L_X - SFR$  relation for star-forming galaxies without AGN,  $\log(L_X) = [39.6 \pm 0.4] + \log(SFR)$  (Mineo et al. 2014), with  $L_X$  the full-band luminosity in erg/s and  $SFR$  in  $M_{\odot}/yr$ . This relation is translated to the soft and hard bands by assuming a spectral index of  $\Gamma = 1.8$ : the resultant relation is consistent with the hard-band  $L_X - SFR/M_*$  relation of Lehmer et al. (2010). A few X-ray sources which are undetected in the hard band lie near the soft-band  $L_X - SFR$  relation and might not host AGN, but most have sufficient X-ray luminosities to be robustly considered as having X-ray emission powered by an AGN.

We also performed X-ray stacking of the three samples in the full band, soft band (0.5–2 keV), and hard band using the 4 Ms CDF-S data (Xue et al. 2011). X-ray detected galaxies and galaxies near any detected X-ray source (within twice the soft-band 90% encircled-energy aperture radius of the X-ray source) were excluded from the stacking. The final clumpy, smooth, and intermediate samples used in the stacking contain 40, 38, and 33 galaxies, respectively. We adopted the same stacking procedure as described in Section 3.1 of Luo et al. (2011). Briefly, we extracted total (source plus background) counts for each galaxy within a  $3''$ -diameter circular aperture centered on its optical position. The corresponding background counts within this aperture were determined with a Monte Carlo approach which randomly (avoiding known X-ray sources) places 1000 apertures within a  $1'$ -radius circle of the optical position to measure the mean background. The total counts ( $S$ ) and background counts ( $B$ ) for the stacked sample were derived by summing the counts for individual sources. The net source counts are then given by  $(S - B)$ , and the S/N is calculated as  $(S - B)/\sqrt{B}$ . A stacked signal is considered undetected if it has a binomial no-source probability of  $P_b > 0.01$  (equivalent to  $S/N \lesssim 2.6\sigma$ ): for these sources we derive 90% confidence upper limits using the Bayesian method of Kraft (Burrows & Nousek). Aperture corrections were applied when converting the source count rates to fluxes and luminosities.

The stacked luminosities are shown with the median SFR of each subset in Figure 12. The small number of objects in each morphology subset means that none are well-detected in the hard band, and only the clumpy and smooth stacks are detected in the soft-band. Due to these poor hard band detections, the hardness ratios are unconstrained in all three stacks. The stacked X-ray

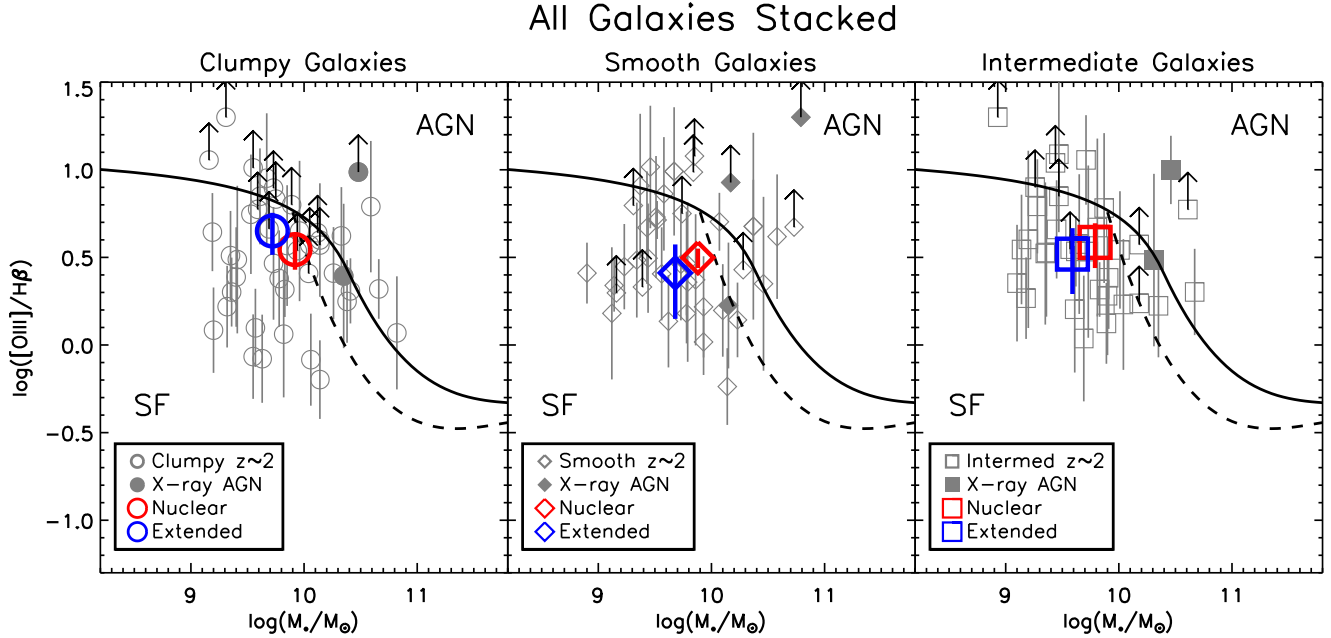


FIG. 10.— The nuclear and extended line ratios of stacked clumpy, smooth, and intermediate morphology galaxies. These line ratios are placed in the MEx diagram using the median  $M_*$  of each stack, with a small artificial offset between the nuclear and extended points. The integrated values for individual galaxies, seen in Figure 7, are shown in gray. Similar nuclear and extended line ratios are seen in all three panels, suggesting that none of the morphology classes have dominant nuclear AGN populations.

TABLE 3  
X-RAY DATA: DETECTIONS AND STACKED NON-DETECTIONS

Galaxy ID	Redshift	$f(0.5-2 \text{ keV})$ ( $\text{erg s}^{-1} \text{ cm}^{-2}$ )	$f(2-8 \text{ keV})$ ( $\text{erg s}^{-1} \text{ cm}^{-2}$ )	$f(0.5-8 \text{ keV})$ ( $\text{erg s}^{-1} \text{ cm}^{-2}$ )	Classification
8206	1.99	$2.24 \times 10^{-17}$	$< 1.02 \times 10^{-16}$	$< 7.13 \times 10^{-17}$	Galaxy
8409	1.82	$2.26 \times 10^{-17}$	$< 1.21 \times 10^{-16}$	$5.18 \times 10^{-17}$	AGN
9258	2.02	$1.64 \times 10^{-17}$	$< 1.05 \times 10^{-16}$	$< 6.58 \times 10^{-17}$	Galaxy
9474	2.12	$2.59 \times 10^{-17}$	$< 1.39 \times 10^{-16}$	$7.37 \times 10^{-17}$	Galaxy
10493	1.83	$8.00 \times 10^{-17}$	$2.11 \times 10^{-16}$	$2.89 \times 10^{-16}$	AGN
6278	1.54	$4.70 \times 10^{-17}$	$6.58 \times 10^{-16}$	$6.75 \times 10^{-16}$	AGN
9493	1.47	$2.72 \times 10^{-17}$	$< 1.14 \times 10^{-16}$	$6.64 \times 10^{-17}$	Galaxy
10650	1.31	$1.28 \times 10^{-16}$	$1.33 \times 10^{-16}$	$2.56 \times 10^{-16}$	AGN
16985	1.73	$2.99 \times 10^{-16}$	$3.95 \times 10^{-15}$	$4.03 \times 10^{-15}$	AGN
9245	2.07	$1.59 \times 10^{-17}$	$9.04 \times 10^{-17}$	$8.01 \times 10^{-17}$	AGN
18315	2.32	$1.57 \times 10^{-16}$	$6.75 \times 10^{-16}$	$8.18 \times 10^{-16}$	AGN
Stacked Clumpy	–	$4.3 \pm 0.9 \times 10^{-18}$	$< 1.1 \times 10^{-17}$	$9.2 \pm 2.8 \times 10^{-18}$	
Stacked Smooth	–	$4.0 \pm 0.9 \times 10^{-18}$	$< 1.6 \times 10^{-17}$	$8.8 \pm 2.9 \times 10^{-18}$	
Stacked Intermediate	–	$< 4.5 \times 10^{-18}$	$< 9.3 \times 10^{-18}$	$< 9.1 \times 10^{-18}$	
Stacked Clumpy MEx AGN	–	$5.2 \pm 1.7 \times 10^{-18}$	$< 2.4 \times 10^{-17}$	$13.9 \pm 5.1 \times 10^{-18}$	
Stacked Smooth MEx AGN	–	$< 5.2 \times 10^{-18}$	$< 2.6 \times 10^{-17}$	$< 17.7 \times 10^{-18}$	
Stacked Intermediate MEx AGN	–	$< 4.6 \times 10^{-18}$	$< 3.3 \times 10^{-17}$	$< 15.7 \times 10^{-18}$	

NOTE. — X-ray fluxes and AGN/galaxy classifications from Xue et al. (2011). X-ray stacking following the method in Luo et al. (2011).

luminosities (and upper limits) for all three samples lie only marginally above the  $L_X - SFR$  line for SF galaxies, indicating a weak or sub-dominant AGN contribution in the X-ray undetected galaxies. This is consistent with the location of most galaxies in the star-forming region of the MEx diagram (Figure 7), and with the lack of nuclear AGN in the resolved line ratios among all galaxies (Figure 10). We also stack the MEx AGNs in each morphology class, but the numbers of objects are too small to make any meaningful conclusions.

Clumpy, smooth, and intermediate galaxies all have

similar detected X-ray AGN fractions ( $\sim 5\%$ ) and stacked X-ray luminosities for undetected sources ( $\log(L_X) \sim 41.4$ ). In agreement with the spatially resolved line ratios, the X-ray data show essentially no differences for clumpy, smooth, and intermediate morphology galaxies at  $z \sim 2$ .

#### 4. DISCUSSION

Both spatially resolved line ratios and X-ray data (detections and stacked non-detections) indicate that there is little or no difference in AGN fraction between clumpy galaxies and those with smoother morphologies. While

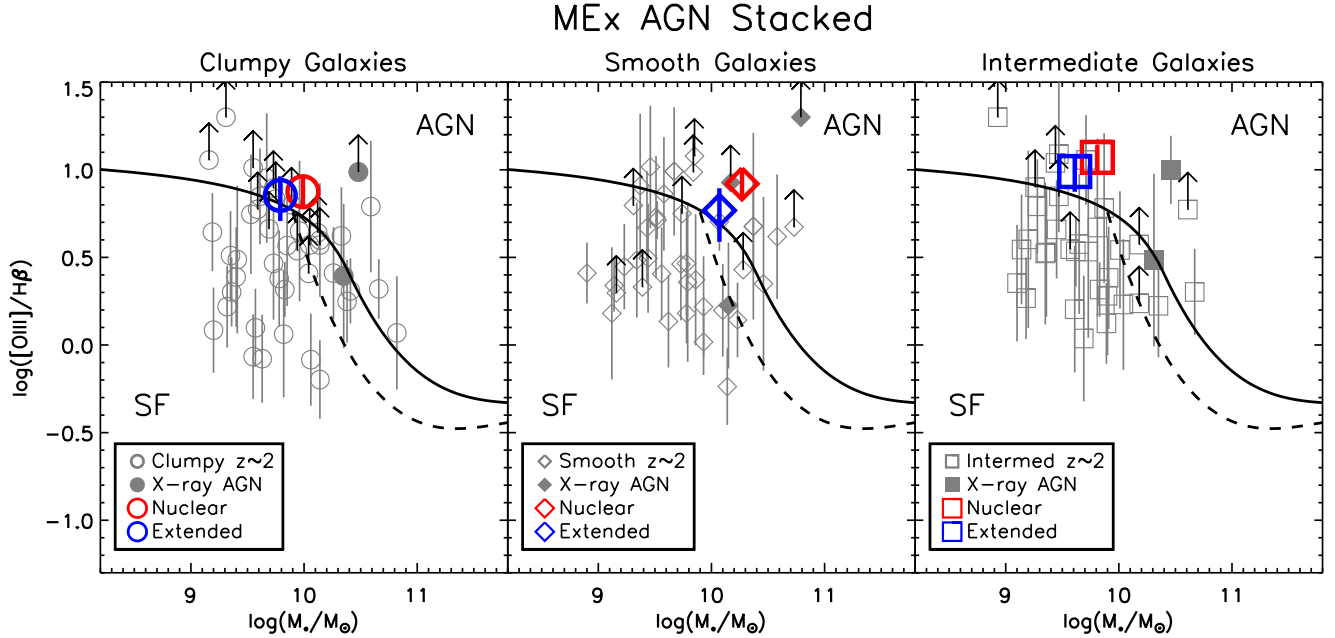


FIG. 11.— The nuclear and extended line ratios of the galaxies identified as AGN on the MEx diagram, stacked in each of the clumpy, smooth, and intermediate morphology classes. As in Figure 10, we place the line ratios in the MEx diagram using the median  $M_*$  of each stack (with a small artificial offset between the nuclear and extended points). Smooth and intermediate MEx-classified AGNs have significantly higher nuclear ratios, suggesting that they are indeed likely to host AGN in their centers. However clumpy MEx AGNs have only marginally higher line ratios in their nuclear region, and much of their AGN-like  $[\text{OIII}]/\text{H}\beta$  ratios comes from extended phenomena like shocks or high-ionization star formation. The spatially resolved line ratios of stacked MEx AGN in each morphology class suggest that clumpy galaxies may actually be less likely to host nuclear AGNs than smoother galaxies.

integrated line ratios in the MEx method suggest a slightly higher AGN fraction among clumpy galaxies, the lack of a nuclear AGN signature suggests that this is due to extended phenomena like dense star-forming clumps rather than black hole growth. Galaxies at  $1.3 < z < 2.4$  in each morphology category have similar AGN fractions of  $\sim 5\text{--}30\%$ , depending on whether X-ray data or spatially resolved line ratios are used for AGN selection.

We discuss several implications of these results below.

#### 4.1. Off-Nuclear AGN in Clumpy Galaxies?

In Section 3.2 we argued that the high  $[\text{OIII}]/\text{H}\beta$  ratio in the extended regions of clumpy galaxies indicates shocks or high-ionization HII regions rather than AGN activity (see also Rich, Kewley & Dopita 2011; Newman et al. 2014; Rich, Kewley & Dopita 2014). However, it is instead possible that some clumpy galaxies host off-nuclear AGN (e.g. Schawinski et al. 2011, 2014). We test for the presence of off-nuclear AGN by creating a 2D stack of clumpy galaxies classified as MEx-AGNs, centering on the  $[\text{OIII}]$  emission lines rather than the continuum trace. The brightest knot of  $[\text{OIII}]$  emission would be most likely to correspond to any off-nuclear AGN<sup>17</sup>. The “nuclear” region of the  $[\text{OIII}]$ -centered stack corresponds to the brightest  $[\text{OIII}]$  knots rather than the galaxy center, and should therefore be where off-nuclear AGNs are most likely to reside.

Figure 13 compares the nuclear and extended  $[\text{OIII}]/\text{H}\beta$  ratios for the continuum-centered stack with the  $[\text{OIII}]$ -centered stack of clumpy galaxies. The right

panel suggests that the brightest  $[\text{OIII}]$  knots are somewhat less likely to host AGNs than the galaxy centers. The lack of widespread off-nuclear AGNs is also supported by the X-ray data, which indicate that clumpy galaxies do not host a greater number of X-ray AGNs (whether nuclear or off-nuclear) than smoother mass-matched galaxies. We conclude that there is unlikely to be a large population of off-nuclear AGNs in clumpy galaxies misclassified by the spatially resolved line ratio method.

#### 4.2. Comparison to Lower Redshift

At first glance, our  $z \sim 1.85$  result is in apparent contrast to the preference for AGN in clumpy galaxies at  $z \sim 0.7$  observed by Bournaud et al. (2012). Our clumpy galaxy sample has very similar images and morphologies to theirs, as seen in a comparison of Figure 3 with Figure 4 of Bournaud et al. (2012). And although we study a much larger sample (three times more clumpy galaxies), Bournaud et al. (2012) performed a comprehensive bootstrap analysis which indicates that sample size is very unlikely to lead to the difference. Our studies differ greatly, however, in the comparison samples of smooth galaxies.

Bournaud et al. (2012) required that both their clumpy and smooth galaxy samples be extended disks. Meanwhile we impose no requirements on morphology beyond the clumpiness classification, and Figure 14 demonstrates that our  $z \sim 2$  clumpy and smooth galaxies are quite different in size and Sérsic (1968) index. These quantities were measured using GALFIT (Peng et al. 2010) and presented by van der Wel et al. (2012). Clumpy galaxies are much more likely to be extended disks, with a median semi-major axis of  $0''.46$

<sup>17</sup> Our assumption that the brightest  $[\text{OIII}]$  knot corresponds to an AGN is inaccurate if there is large-scale dust asymmetrically obscuring an AGN narrow-line region.

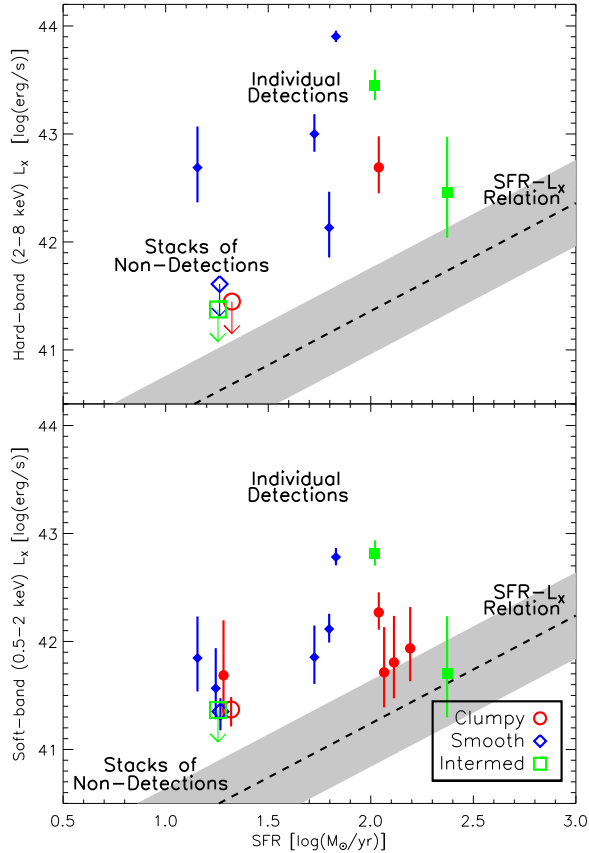


FIG. 12.— Hard-band (top panel) and soft-band (bottom panel) X-ray luminosities versus star formation rates, for both individually detected galaxies (solid points) and stacked non-detections (open points) among the three morphology types. The dashed lines indicate the  $L_X - SFR$  relation for star-forming galaxies without AGN from Mineo et al. (2014), and the gray shaded region indicates the relation’s  $1\sigma$  errors. Most individually detected sources have sufficiently high (hard) X-ray detections to be AGN, although the stacked data suggest only weak AGN emission in the X-ray non-detections. In both detected sources and stacked data, there are no significant differences in X-ray AGN likelihood data between clumpy, smooth, and intermediate morphology galaxies.

and 41/44 galaxies having disk-dominated Sérsic indices ( $n < 2.5$ ). The smooth galaxies are still mostly disk-dominated, as 30/41 have  $n < 2.5$ , but they are significantly smaller (with a median semi-major axis of  $0''.20$ ) and have higher Sérsic indices.

It is interesting that so few smooth extended disks are observed in CANDELS and 3D-HST. The data are sensitive to the  $z \sim 2$  star-forming main sequence at  $M_*/M_\odot > 10^{9.8}$  (Figure 6), and so if smooth extended disks exist they must be low-mass and/or weakly star-forming. Kassin et al. (2012) and Elmegreen & Elmegreen (2014) argue that ordered disks are rare in  $z > 1$  galaxies of any mass, suggesting that the lack of smooth extended disks at  $z \sim 2$  is a consequence of galaxy evolution rather than selection effects. Regardless, the lack of smooth extended disks at  $z \sim 2$  means we cannot perform the same comparison between clumpy and smooth extended disks as Bournaud et al. (2012) at  $z \sim 0.7$ . Instead we conclude that clumpy extended galaxies have the same AGN fraction as more compact and higher-Sérsic smooth galaxies matched in stellar mass.

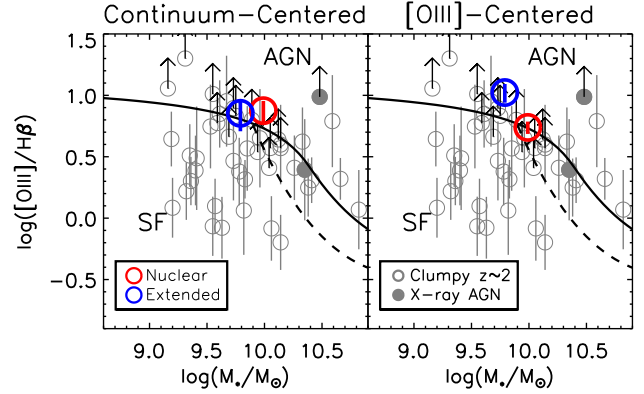


FIG. 13.— Nuclear and extended line ratios of clumpy galaxies classified as MEx AGNs. The left panel uses a stacked spectrum from galaxies centered on their continuum trace, while the right panel tests for the presence of off-nuclear AGNs with a stacked spectrum constructed by centering each galaxy on the brightest knot of [OIII] emission. There is no evidence for a large population of off-nuclear AGNs in clumpy galaxies, which would have manifested as a higher “nuclear” line ratio in the [OIII]-centered stack.

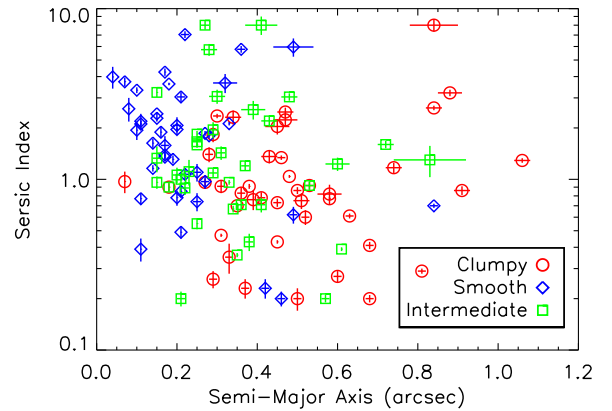


FIG. 14.— Sérsic index versus size (semi-major axis) for the clumpy, smooth, and intermediate galaxies. The smooth and intermediate galaxies are generally smaller than the clumpy galaxies, and tend to have more prominent bulges (although  $>70\%$  are still disk-dominated with  $n < 2.5$ ).

#### 4.3. Fueling AGNs at $z \sim 2$

Our results demonstrate that clumpy galaxies at  $z \sim 2$  are no more likely to host AGNs than are smooth galaxies of the same stellar mass and similar star formation rate. What does this indicate about AGN fueling modes at  $z \sim 2$ ?

Dekel & Burkert (2014) argue that compact star-forming galaxies (also called blue nuggets) might actually be constructed by a history of violent disk instabilities. Our smooth galaxies, which tend to be more compact and bulgy than the clumpy extended disks, have sizes and Sérsic indices consistent with this category (see also Ceverino et al. 2014). The observed similarity in AGN fraction between  $z \sim 2$  clumpy and smooth galaxies would then indicate that nuclear inflow onto the AGN must persist until after the galaxy becomes stable and the star-forming clumps are no longer visible. In this scenario the violent disk instabilities are responsible for building a gas reservoir in the galaxy’s center. Since

the actual nuclear inflow onto the AGN persists into the smooth compact galaxy phase, it must not depend on violent instabilities in the larger disk. So while the gas reservoir is deposited by violent disk instabilities, the AGN fueling within  $\sim 1$  kpc must instead be driven by secular processes.

On the other hand, the disk-dominated nature of the smooth galaxies might imply that they are unlikely to have experienced violent mixing in the past from extreme disk instabilities (or major mergers). It is also not clear that the smooth galaxies are older than the clumpy galaxies, given their similar position in the SFR- $M^*$  plane (excepting the most massive galaxies: see Figure 6). This might imply that even the large-scale fueling occurs via secular processes, perhaps due to stochastic turbulence from the high gas fractions which are common in  $z \sim 2$  galaxies (Tacconi et al. 2010). Indeed, Hopkins, Kocevski, & Bundy (2014) predict that this turbulence-driven stochastic fueling is the dominant mode of SMBH growth for  $z \sim 2$  galaxies with  $M_{BH} < 10^7 M_\odot$  (or  $M_* < 10^{10} M_\odot$ ): the same mass range occupied by much of our sample. Assuming that the smooth and clumpy morphologies in our sample trace different fueling modes, then our data best support the scenario of Bellovary et al. (2013), where AGN growth depends not on fueling mode, but on gas fraction.

## 5. SUMMARY

We use spatially resolved line ratios and X-ray data to demonstrate that  $z \sim 1.85$  clumpy galaxies are no

more likely to host AGNs than are smoother galaxies at the same redshift. While integrated line ratios indicate a higher AGN fraction in clumpy galaxies, the spatially resolved emission lines show that this is likely due to extended phenomena (like shocks or high-ionization HII regions) rather than nuclear (or off-nuclear) AGNs. While the smooth galaxies have the same masses and nearly the same star formation rates, they are somewhat smaller and not quite as disk-dominated as the clumpy galaxies. Whatever process drives AGN fueling in the smooth galaxies is just as efficient as are violent disk instabilities in clumpy galaxies at  $z \sim 2$ .

We thank Frederic Bournaud for valuable discussion which significantly improved this work. Support was provided by NASA through Hubble Fellowship grant #51330 awarded by the Space Telescope Science Institute, which is operated by the Association of Universities for Research in Astronomy, Inc., for NASA under contract NAS 5-26555. JRT and the authors from UCSC also acknowledge support from NASA HST grants GO-12060.10-A and AR-12822.03, Chandra grant G08-9129A, and NSF grant AST-0808133. SJ acknowledges financial support from the E.C. through an ERC grant StG-257720. This work made use of the Rainbow Cosmological Surveys Database, which is operated by the Universidad Complutense de Madrid (UCM), partnered with the University of California Observatories at Santa Cruz (UCO/Lick, UCSC).

## REFERENCES

- Aird, J., Nandra, K., Laird, E. S. et al. 2010, MNRAS, 401, 2531  
 Baldwin, J. A., Phillips, M. M. & Terlevich, R. 1981, PASP, 93, 5  
 Barro, G., Faber, S. M., Perez-Gonzalez, P. G. et al. 2013, ApJ, 765, 104  
 Bellovary, J., Brooks, A., Volonteri, M., Governato, F., Quinn, T., & Wadsley, J. 2013, ApJ, 779, 136  
 Bennert, V. N., Auger, M. W., Treu, T., Woo, J.-H. & Malkan, M. A. 2011, ApJ, 742, 107  
 Bertin, E. & Arnouts, S. 1996, A&AS, 117, 393  
 Bournaud, F. Daddi, E., Elmegreen, B. G. et al. 2008, A&A, 486, 741  
 Bournaud, F. Dekel, A., Teyssier, R., Cacciato, M., Daddi, E., Juneau, S. & Shankar, F. 2011, ApJ, 741, 33  
 Bournaud, F., Juneau, S., Le Floch, E. et al. 2012 ApJ, 757, 81  
 Bournaud, F., Perret, V., Renaud, F. et al. 2014 ApJ, 780, 57  
 Brammer, G. B., Sánchez-Janssen, R., Labbé, I. et al. 2012, ApJS, 200, 13  
 Brammer, G. B., van Dokkum, P. G., Illingworth, G. D., Bouwens, R. J., Labbé, I., Franx, M., Momcheva, I. & Oesch, P. A. 2013, ApJ, 765, 2  
 Brinchmann, J., Pettini, M. & Charlot, S. 2008, MNRAS, 385, 769  
 Bruzual, G. & Charlot, S. 2003, MNRAS, 344, 1000  
 Calzetti, D. 2001, PASP, 113, 1449  
 Ceverino, D., Dekel, A., Mandelker, N., Bournaud, F., Burkert, A., Genzel, R. & Primack, J. 2012, MNRAS, 420, 3490  
 Ceverino, D., Dekel, A. et al. in prep.  
 Chabrier, G. 2003, PASP, 115, 763  
 Chen, C.-T. J., Hickox, R. C., Alberts, S. et al. 2013, ApJ in press (arXiv:1306.1227)  
 Cisternas, M., Jahnke, K., Bongiorno, A. et al. 2011, ApJ, 741, 11  
 Cowie, L. L., Hu, E. M., Songaila, A. 1995, AJ, 110, 1576  
 Daddi, E., Dickinson, M., Morrison, G. et al. 2007, ApJ, 670, 156  
 Daddi, E., Bournaud, F., Walter, F., Dannerbauer, H., Carilli, C. L., Dickinson, M., Elbaz, D., Morrison, G. E., Riechers, D., Onodera, M., Salmi, F., Krips, M. & Stern, D. 2010, ApJ, 713, 686  
 Dahlen, T., Mobasher, B., Dickinson, M. et al. 2010, ApJ, 724, 425  
 Dahlen, T., Mobasher, B., Faber, S. M. et al. 2013, ApJ, 775, 93  
 Dekel, A. & Birnboim, Y. 2006, MNRAS, 368, 2  
 Dekel, A., Birnboim, Y., Engel, G. et al. 2009, Nature, 457, 451  
 Dekel, A., Sar, R. & Ceverino, D. 2009, ApJ, 703, 785  
 Dekel, A., Zolotov, A., Tweed, D., Cacciato, M., Ceverino, D. & Primack, J. R. 2013, MNRAS, 435, 999  
 Dekel, A. & Burkert, A. 2014, MNRAS, 438, 1870  
 Di Matteo, T., Springel, V., & Hernquist, L. 2005, Nature, 433, 604  
 Donley, J. L., Koekemoer, A. M., Brusa, M. et al. 2012, ApJ, 748, 142  
 Ellison, S. L., Mendel, J. T., Scudder, J. M., Patton, D. R. & Palmer, M. J. D. 2011, MNRAS, 430, 3128  
 Elmegreen, D. M., Elmegreen, B. G. & Hirst, A. C. 2004, ApJ, 604, 21  
 Elmegreen, D. M. & Elmegreen, B. G. 2014, ApJ, 781, 11  
 Forbes, J. C., Krumholz, M. R., Burkert, A. & Dekel, A. 2014, MNRAS, 438, 1552  
 Förster Schreiber, N. M., Genzel, R., Bouché, N. et al. 2009, ApJ, 706, 1364  
 Gabor, J. M., Impey, C. D., Jahnke, K. et al. 2009, ApJ, 691, 705  
 Genzel, R., Newman, S., Jones, T. et al. 2011, ApJ, 733, 101  
 Giavalisco, M., Ferguson, H. C., Koekemoer, A. M. et al. 2004, ApJ, 600, 93  
 Grogin, N. A., Conselice, C. J., Chatzichristou, E. et al. 2005, ApJ, 627, 97  
 Grogin, N. A., Kocevski, D. D., Faber, S. M. et al. 2011, ApJS, 197, 35  
 Gültekin, K., Richstone, D. O., Gebhardt, K. et al. 2009, ApJ, 698, 198  
 Guo, Y., Giavalisco, M., Ferguson, H. C., Cassata, P. & Koekemoer, A. M. 2012, ApJ, 757, 120  
 Guo, Y., Ferguson, H. C., Giavalisco, M. et al. 2013, ApJS, 207, 42  
 Guo, Y., Ferguson, H. C., Bell, E. F. et al. 2014, ApJ submitted  
 Hainline, K. N., Hickox, R., Greene, J. E., Myers, A. D. & Zakamska, N. L. 2013, ApJ, 774, 145  
 Harrison, C. M., Alexander, D. M., Mullaney, J. R. et al. 2012, ApJ, 760, 15

- Hernquist, L. 1989, *Nature*, 340, 687  
Hopkins, A. M. & Beacom, J. F. 2006, *ApJ*, 651, 142  
Hopkins, P. F., Hernquist, L., Cox, T. J., DiMatteo, T., Robertson, B. & Springel, V. 2008, *ApJS*, 175, 356  
Hopkins, P. F., Kereš, D., Murray, N., Quataert, E. & Hernquist, L. 2012, *MNRAS*, 427, 968  
Hopkins, P. F., Kereš, D. & Murray, N. 2013, *MNRAS*, 432, 2639  
Hopkins, P. F., Kocevski, D. D. & Bundy, K. 2014, *MNRAS* submitted (arXiv:1309.6321)  
Jahnke, K., Bongiorno, A., Brusa, M. et al. 2009, *ApJ*, 706, 215  
Juneau, S., Dickinson, M., Alexander, D. M. & Salim, S. 2011, *ApJ*, 736, 104  
Juneau, S., Bournaud, F., Charlot, S. et al. 2014, *ApJ*, 788, 88  
Kartaltepe, J., Mozena, M., Kocevski, D. D. et al. 2014, *ApJ* submitted (arXiv:1401.2455)  
Kassin, S. A., Weiner, B. J., Faber, S. M. et al. 2012, *ApJ*, 758, 106  
Kauffmann, G., Heckman, T. M., White, S. D. M. et al. 2003a, *MNRAS*, 341, 33  
Kauffmann, G., Heckman, T. M., Tremonti, C. et al. 2003b, *MNRAS*, 346, 1055  
Kauffmann, G. & Heckman, T. M. 2009, *MNRAS*, 397, 135  
Kennicutt, R. C., Jr. 1998, *ARA&A*, 36, 189  
Kereš, D., Katz, N., Weinberg, D. H., & Davé, R. 2005, *MNRAS*, 363, 2  
Kewley, L. J., Groves, B., Kauffmann, G. & Heckman, T. 2006, *MNRAS*, 372, 961  
Kewley, L. J., Maier, C., Yabe, K., Ohta, K., Akiyama, M., Dopita, M. A. & Yuan, T. 2013, *MNRAS*, 774, 100  
Kocevski, D. D., Faber, S. M., Mozena, M. et al. 2012, *ApJ*, 744, 148  
Koekemoer, A. M., Faber, S. M., Ferguson, H. C. et al. 2011, *ApJS*, 197, 36  
Koss, M., Mushotzky, R., Veilleux, S. & Winter, L. 2010, *ApJ*, 716, 125  
Kraft, R. P., Burrows, D. N. & Nousek, J. A. 1991, *ApJ*, 374, 344  
Kümmel, M., Walsh, J. R., Pirzkal, N., Kuntschner, H. & Pasquali, A. 2009, *PASP*, 121, 59  
Lehmer, B. D., Alexander, D. M., Bauer, F. E. et al. 2010, *ApJ*, 724, 559  
Liu, X., Shapley, A. E., Coil, A. L., Brinchmann, J. & Ma, C.-P. 2008, *ApJ*, 678, 758  
Luo, B., Brandt, W. N., Xue, Y. Q. et al. 2011, *ApJ*, 740, 37  
Magorrian, J., Tremaine, S., Richstone, D. O. et al. 1998, *AJ*, 115, 2285  
Mandelker, N., Dekel, A., Ceverino, D., Tweed, D., Moody, C. E. & Primack, J. 2014, *MNRAS* submitted (arXiv:1311.0013)  
Masters, D. & Capak, P. 2011, *PASP*, 123, 638  
Mineo, S., Gilfanov, M. & Sunyaev, R. 2014, *MNRAS*, 437, 1698  
Moody et al. 2014 in prep  
Mullaney, J. R., Daddi, E., Béthermin, M. et al. 2012, *ApJ*, 753, 30  
Newman, S. F., Buschkamp, P. & Genzel, R. et al. 2014, *ApJ*, 781, 21  
Noeske, K. G., Weiner, B. J., Faber, S. M. et al. 2007, *ApJ*, 660, 43  
Osterbrock, D. E. & Parker, A. R. 1965, *ApJ*, 141, 892  
Peng, C. Y., Impey, C. D., Rix, H.-W. et al. 2006, *ApJ*, 640, 114  
Peng, C. Y., Ho, L. C., Impey, C. D. & Rix, H.-W. 2010, *AJ*, 139, 2097  
Ravindranath, S., Giavalisco, M., Ferguson, H. C. et al. 2006, *ApJ*, 652, 963  
Rich, J. A., Kewley, L. J. & Dopita, M. A. 2011, *ApJ*, 734, 87  
Rich, J. A., Kewley, L. J. & Dopita, M. A. 2014, *ApJ*, 781, 12  
Rosario, D. J., Santini, P., Lutz, D. et al. 2013, *ApJ*, 771, 63  
Rosario, D. J., Trakhtenbrot, B., Lutz, D. et al. 2013, *A&A*, 560, 72  
Sanders, D. B., Soifer, B. T., Elias, J. H., Madore, B. F., Matthews, K., Neugebauer, G. & Scoville, N. Z. 1988, *ApJ*, 325, 74  
Schawinski, K., Urry, M., Treister, E., Simmons, B., Natarajan, P. & Glikman, E. 2011, *ApJ*, 743, 37  
Schawinski, K. et al. 2014, in prep.  
Sérsic, J. L. 1968, *Atlas de galaxias australes* (Cordoba: Observatorio Astronomico)  
Seyfert, C. K. 1943, *ApJ*, 97, 28  
Shapiro, K. L., Genzel, R., Förster Schreiber, N. M. et al. 2008, *ApJ*, 682, 231  
Shlosman, I. & Noguchi, M. 1993, *ApJ*, 414, 474  
Storey, P. J. & Zeippen, C. J. 2000, *MNRAS*, 312, 813  
Tacconi, L. J. et al. 2010, *Nature*, 463, 781  
Treister, E., Schawinski, K., Urry, C. M. & Simmons, B. D. 2012, *ApJ*, 758, 39  
Tremonti, C. A. et al. 2004, *ApJ*, 613, 898  
Trump, J. R., Impey, C. D., Kelly, B. C. et al. 2011, *ApJ*, 733, 60  
Trump, J. R., Weiner, B. J., Scarlata, C. et al. 2011a, *ApJ*, 743, 144  
Trump, J. R. 2011b, Conference Proceedings for Galaxy Mergers in an Evolving Universe (Hualien, Taiwan); Editors: Wei-Hsin Sun, Nick Scoville (arXiv:1112.3970)  
Trump, J. R., Konidakis, N. P., Koo, D. C. et al. 2013a, *ApJ*, 763, 6  
Trump, J. R., Hsu, A. D., Fang, J. J. et al. 2013b, *ApJ*, 763, 133  
van der Laan, T. P. R., Schinnerer, E., Boeker, T. & Armus, L. 2013, *A&A*, 560, 99  
van der Wel, A., Bell, E. F., Häußler, B. et al. 2012, *ApJS*, 203, 24  
Veilleux, S. & Osterbrock, D. E. 1987, *ApJS*, 63, 295  
Wright, S. A., Larkin, J. E., Graham, J. R. & Ma, C.-P. 2010, *ApJ*, 711, 1291  
Wuyts, S., Förster Schreiber, N. M., van der Wel, A. et al. 2011, *ApJ*, 742, 96  
Wuyts, S., Förster Schreiber, N. M., Genzel, R. et al. 2012, *ApJ*, 753, 114  
Xue, Y. Q., Luo, B., Brandt, W. N. et al. 2011, *ApJS*, 195, 10  
Xue, Y. Q., Wang, S. X., Brandt, W. N. et al. 2012, *ApJ*, 758, 129  
Yan, R. & Blanton, M. R. 2012, *ApJ*, 747, 61  
York, D. G. et al. 2000, *AJ*, 120, 1579

## APPENDIX

## GALAXY IMAGES

Color-composite *HST iJH* images of all clumpy, smooth, and intermediate galaxies are shown in Figures 15, 16, and 17.

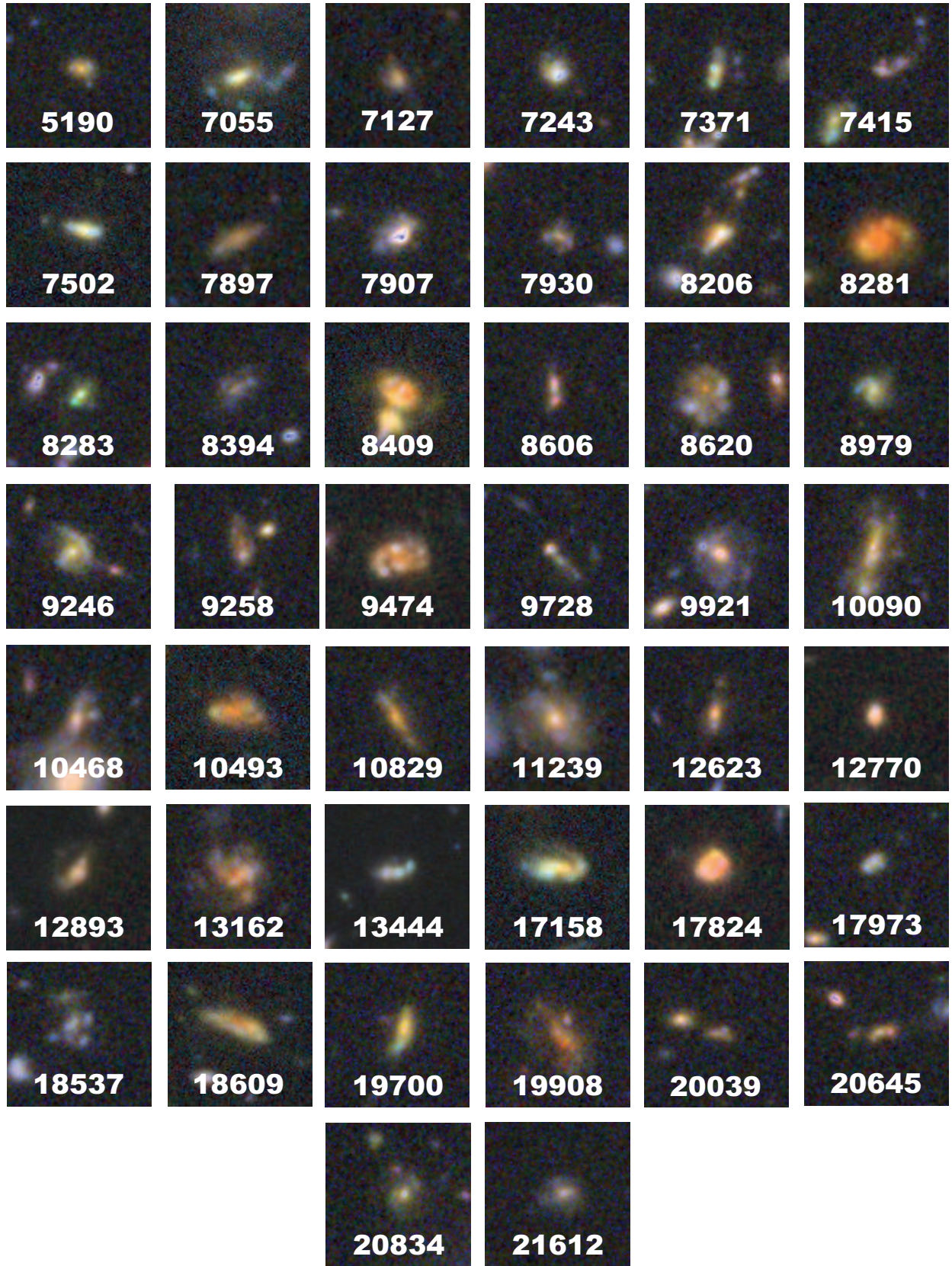


FIG. 15.— Images of the 44 clumpy galaxies. Each thumbnail is  $5''$  on a side, and is a color-composite of the *HST* ACS *i* and WFC3 *JH* bands.

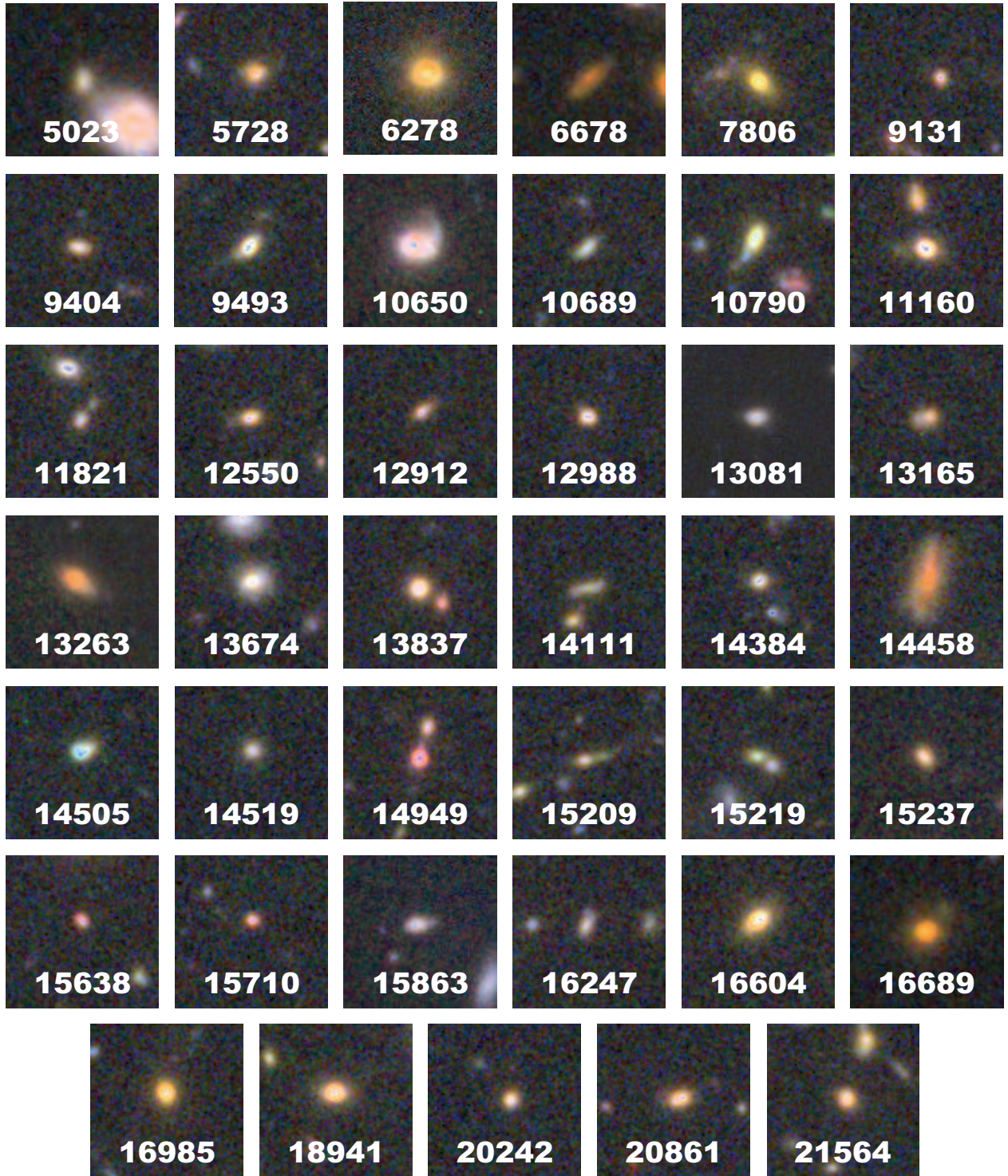


FIG. 16.— Color-composite  $iJH$   $5'' \times 5''$  images of the 41 smooth galaxies.



FIG. 17.— Color-composite *iJH*  $5'' \times 5''$  images of the 35 intermediate-morphology galaxies.